(NASA-CR-163968) SECONDARY ELECTRON EMISSION FROM ELECTRICALLY CHARGED FLUORINATED-ETHYLENE-PROPYLENE TEFLON FOR NORMAL AND NON-NORMAL ELECTRON INCIDENCE M.S. Thesis (Pennsylvania State Univ.)

N81-18892

G3/76

Unclas
41091

The Pennsylvania State University

Electrical Engineering Department

University Park, Pennsylvania 16802

SECONDARY ELECTRON EMISSION FROM ELECTRICALLY CHARGED FLUORINATED-ETHYLENE-PROPYLENE TEFLON FOR NORMAL AND NON-NORMAL ELECTRON INCIDENCE

Technical Report

NASA Grant No. NSG-3166

Paul A. Budd

March 1981

The Pennsylvania State University

Electrical Engineering Department

University Park, Pennsylvania 16802

SECONDARY ELECTRON EMISSION FROM ELECTRICALLY CHARGED FLUORINATED-ETHYLENE-PROPYLENE TEFLON FOR NORMAL AND NON-NORMAL ELECTRON INCIDENCE

Technical Report

NASA Grant No. NSG-3166

Paul A. Budd

March 1981

The Pennsylvania State University

The Graduate School

Department of Electrical Engineering

Secondary Electron Emission from Electrically Charged Fluorinated-Ethylene-Propylene Teflon for Normal and Non-Normal Electron Incidence

A Thesis in

Electrical Engineering

by

Paul Arthur Budd

Submitted in Partial Fulfillment
of the Requirements
for the Degree of

Master of Science

March 1981

ABSTRACT

The secondary electron emission coefficient was measured for a charged polymer (FEP-Teflon) with normally and obliquely incident primary electrons. Theories of secondary emission are reviewed and the experimental data is compared to these theories. Results were obtained for angles of incidence up to 60° in normal electric fields of 1500 V/mm. Additional measurements in the range from 50° to 70° were made in regions where the normal and tangential fields were approximately equal.

In these experiments the surface of the dielectric was irradiated with a diffuse monoenergetic electron beam until a stable charge distribution was observed. When a thin (0.15 mm x 1 mm) collimated electron beam was injected into the specimen's environment with an energy equal to 80% of the surface potential, the beam deflected and struck detector wires as it left the chamber which contained the specimen. The initial input angles and measured output point of the electron beam could be analyzed with computer simulations in order to determine the field within the chamber. The computer simulations used conformal mapping, a Green's integral, and numerical integration to trace particle trajectories.

When the field is known, the trajectories can be calculated for impacting electrons having various energies and angles of incidence. There was close agreement between the experimental results and the commonly assumed theoretical model in the presence of normal electric fields for angles of incidence up to 60°. High-angle

results obtained in the presence of tangential electric fields did not agree with the theoretical models.

TABLE OF CONTENTS

CHAPTER Page

LIST OF TABLES

Table | Page

LIST OF FIGURES

Figure | Page

LIST OF SYMBOLS

α - The angle which the probing beam has with respect to the platform as the beam enters the cylinder. It is defined to be the cylindrical angle of incidence.

β - The tilt of the entering primary beam with respect to the cylinder radius and defined to be the angle of inclination.

γ - The angle which a reflected primary electron beam has with respect to the specimen platform.

δ - The true secondary electron emission coefficient equal to N_s/N_p.

θ - The angle which the probing beam has just prior to impact with the specimen surface.

ϕ - Dummy variable of integration.

σ - The total secondary electron emission coefficient equal to the sum of δ, i, and r.

σ_{max} - The maximum value of the total secondary electron emission coefficient.

a_o - The first coefficient in a Taylor series expansion for the energy loss function with units of eV/cm.

a_1 - The second coefficient in a Taylor series expansion for the energy loss function with units of eV/cm^2.

A - The constant appearing in Whiddington's law with units of $(eV)^2/cm$.

A_o - The peak surface potential (V) at X=0.

A_i - Polynomial coefficients describing the surface potential having the units of volts.

B - Halfwidth of specimen after the conformal mapping.

B_o - Halfwidth of specimen in the original plane.

BV_{CEO} - Breakdown voltage between collector and emitter of T_1.

C_1 - A constant equal to $f(0)AK_1X_s$ having units of energy (eV).

C_2 - A constant, having the units of one over energy (eV^{-1}), appearing in the energy loss function.

C_3 - A unitless constant equal to $C_2X_s|dE/dx|$ used when $|dE/dx|$ is assumed to be constant.

D - This is the deflection factor which has the units of radians/volt and characterizes the deflection of the probing beam as a function of acceleration potential.

DV - The deflection voltage applied to the probing beam.

e - The electronic charge 1.6×10^{-19}C.

E - The energy of a primary electron as it moves through the material.

E_o - This is the energy of a primary electron just before it impacts the surface.

E_1 - Below this energy the emitted electrons are true secondary electrons while above it the remaining electrons are either inelastically or elastically reflected electrons.

$E_{1_{max}}$ - The maximum value of E_1 when probing energies greater than 60eV are used.

E_2 - This energy divides the inelastically (below) from elastically (above) reflected electrons in the secondary energy spectrum curve.

E_c - The critical energy which separates the unity emission points, $E_f - A_o$.

E_{co} - The critical energy for an uncharged specimen.

E_{cond} - The conduction band energy.

E_f - The energy of the electrons leaving the flood gun.

E_g - The energy gap of a material, $E_{cond} - E_{val}$

E_{max} - The secondary energy at which σ_{max} occurs.

E_p - The primary probing beam energy as it enters the cylinder.

E_u - Electric field component in the u direction.

E_v - Electric field component in the v direction.

E_w - The work function of a material in eV.

E_x - Electric field component in the x direction.

E_y - Electric field component in the y direction.

$\bar{f}$ - The probability of escape for a secondary right at the material surface.

$f(x)$ - The secondary emission probability function.

F - Time step change parameter.

i - Unitless coefficient which is the ratio of the inelastically reflected electrons to the total number of incident electrons.

I - Current in primary beam.

I_1 - TTL inverter 1.

I_2 - TTL inverter 2.

I_{max} - Maximum probe beam current striking a detector wire.

I_{Ni} - Integrals used in evaluating fields and potentials.

K_1 - The inverse of the activation energy required to produce a secondary electron.

K_2 - Primary range equation coefficient having the units of $cm(eV)^{-2}$.

l - Length of platform (12.7 cm).

l_c - Free mean path of a secondary electron before becoming trapped in a trapping center.

L - Diffusion length of secondaries in a material.

m - Non-zero exponent in series expansion of surface potential.

n - The exponent which is used to model the high energy behavior of σ.

$n(x, E_o)$ - The excitation density for secondaries with units of cm^{-1}.

$N(E)$ - The energy spectrum of emitted electrons having the units of $(eV)^{-1}$.

N_e - The number of elastically reflected electrons.

N_i - The number of inelastically reflected electrons.

N_o - The number of electrons remaining in the probing beam charge packet as it moves through the material.

N_p - The total number of primary electrons contained in a probing beam charge packet.

N_s - The number of true secondary electrons emitted from the surface.

$p(x)$ - Probability that a primary electron has been stopped by the material.

$P(X,Y)$, $P'(X)$ - Potential above or on the specimen.

q - Charge to mass ratio.

Q - $R\cos\theta/X_s$.

Q_a - The amount of surface charge present on the specimen surface for an area the size of the probe beam area.

Q_c - The amount of charge (C) detected by the collector.

Q_m - The measured charge (C) released from a discharged specimen when struck by the probing beam.

Q_n - The amount of negative charge (C) deposited locally on a charged specimen by the probing beam ($\sigma < 1$).

Q_o - The average surface charge density (C/cm^2) on the surface of a charged specimen.

Q_p - The total primary charge (C) directed at the specimen in a discrete charge packet.

Q_r - The measured positive charge (C) recorded when the probing beam impacts a charged specimen ($\sigma > 1$).

Q_s - The amount of charge (C) reflected back from the uncharged specimen when struck with a high energy probing beam.

Q_t - The total charge deposited on the entire surface of the specimen when the flood gun is activated.

r - The ratio of elastically reflected electrons N_e to the total primary electrons N_p.

r_o - The radius of the cylinder.

R - The primary range or farthest distance to which a primary may penetrate the surface.

R_b - Base resistor in pulse circuitry.

R_c - Collector resistor in pulse circuitry.

R_f - Filter resistor in pulse circuitry.

R_s - Switch resistor used in pulse circuitry.

S,T - Real and imaginary parts of dZ/dW.

S_1 - Switch one in pulse circuitry.

S_2 - Switch two in pulse circuitry.

t_i - Present time in iterative stepping procedure.

t_p - Pulse width of pulse circuitry.

T - Time step.

T_1 - High voltage transistor used in pulse circuitry.

U,V - Real and imaginary parts of W.

V_1 - Deflection voltage at which I_{max} occurs for a discrete motor drive position.

V_2 - Deflection voltage at which I_{max} occurs for a motor drive position one step beyond the position used to measure V_1.

V_a, V_b, V_d, V_e - Deflection voltages which are measured when the detector wire measures a current of $I_{max}/2$.

V_{dv} - $(V_1 - V_2)$.

V_H - The high voltage used in the pulse circuitry.

V_L - The low voltage used in the pulse circuitry.

W - Complex representation of a point in upper half plane.

x - Perpendicular distance into the dielectric.

X - Distance measured across the dielectric specimen.

$\bar{x}$ - Mean electron escape depth.

X,Y - Real and imaginary parts of Z.

X_o - Specific impact point on surface of specimen.

X_s - Secondary range.

Z - Complex representation of a point in upper half plane.

Subscripts:

i - Present time

h,-h - Half time step ahead or behind.

i+1 - Whole time step ahead.

ACKNOWLEDGMENTS

The author is grateful to Dr. James W. Robinson, who supervised this work and who provided a major contribution. He also thanks Dr. Hai-Sup Lee, Dr. Lynn Carpenter, and Dr. Dale Grimes for the time they spent reading and criticizing this thesis. Finally, the financial support provided by the National Aeronautics and Space Administration under Grant NSG-3166 was greatly appreciated.

CHAPTER I

INTRODUCTION

Spacecraft placed in geosynchronous orbits are subjected to electrical charging by their environment. Overheating of these spacecraft is prevented by equipping them with thermal coatings which are often electrical insulators and which unfortunately become charged in the vacuum environment. This charging phenomenon creates electric fields which, if allowed to become strong enough, will cause surface breakdown. Normal satellite operations and communications can be disrupted by accumulated charges and transient currents; therefore a better understanding of these thermal materials can aid in the design of more reliable spacecraft exteriors with the spacecraft modeling techniques as developed by D. E. Katz et al. (1). The behavior of these thermal materials is the subject of this report and preceding reports (2, 3, 4, 5, 6, 7) from this laboratory.

The software compiled by D. J. Tilley (6) and N. Quoc-Nguyen (7) has been modified by J. W. Robinson (8) to suit the computational needs of this current research project. The work of N. Quoc-Nguyen (7) was mainly experimental and his thesis presented results concerning secondary electron emission from a dielectric film subjected to various normal electric fields and charge densities.

Potential field distributions were obtained by D. J. Tilley (6) from an analysis of measured electron trajectories. Tilley found general solutions to Laplace's equation generated by summing multipole fields using computer programs he compiled.

This paper is an extension of the methods and results presented by these previous researchers. Experiments conducted by this author provided information concerning field distributions and secondary electron emission from a charged dielectric using obliquely incident electrons. The secondary electron emission results presented herein and the results gathered by N. Quoc-Nguyen were for normal electric fields.

A report (8) concerning the software required to process the experimental data was prepared by J. W. Robinson in September of 1980. This complementary report describes the computer programs used in the estimation of field distributions. These approximate potentials were used in determining electron beam trajectories for various angles of incidence.

It was necessary to measure and model the potential distribution across the dielectric surface in order to gather data on secondary emission for obliquely incident electrons. Therefore the first task was to create a system into which electrons could be injected and their exit points measured. A proper choice of the specimen's electrostatic environment yields a geometry which can be modelled with relative mathematical ease. Figure 1 shows the geometry used which was that of a half cylinder with the specimen placed in the center of the bisecting plane. A two-dimensional simulation which employs conformal mapping is used to compute potentials and electric fields within the electrostatic environment. A polynomial representation of the potential distribution is used where the potentials and electric fields are expressed as integrals weighted by the polynomial coefficients.

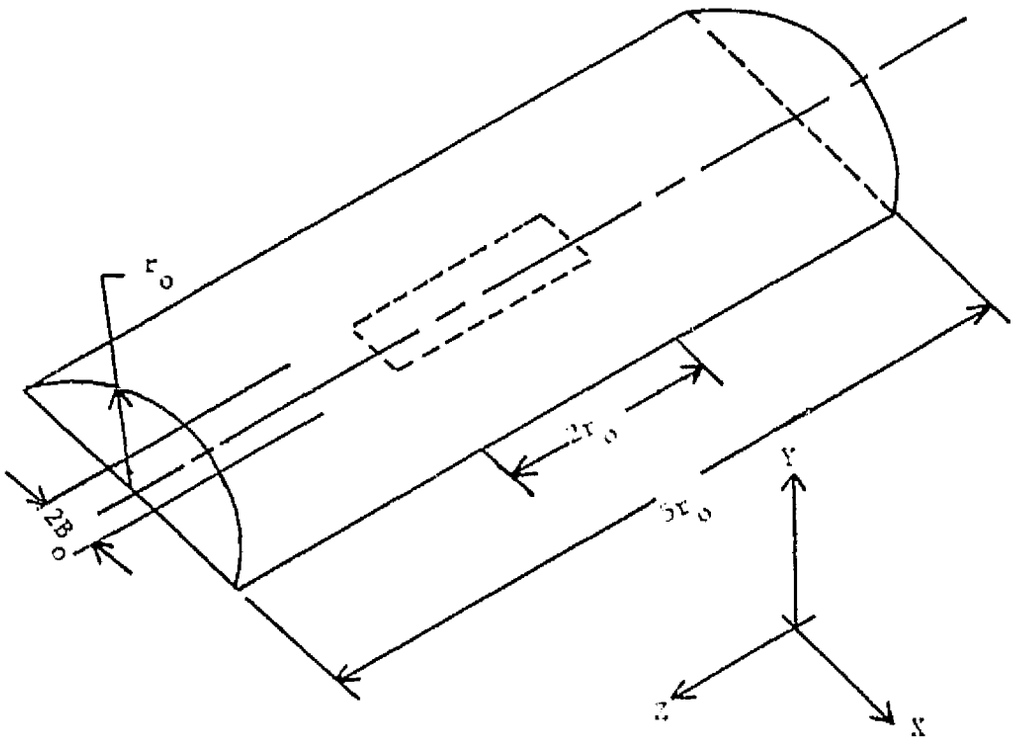

Figure 1. Geometrical representation of the specimen and its environment.

The emphasis of this thesis is mainly experimental in nature, yet a general knowledge of emission mechanics and mathematical models is necessary for one to gain insight into the experimental results. Therefore the remainder of this chapter is devoted to a review of literature on secondary emission from polymers and a number of equations are derived which will be used to compare experimental results with relevant theories.

Phenomenology of Theories for Secondary Emission

Secondary electron emission is the effect by which electrons are emitted from a solid when bombarded by electrons. The mechanisms are as follows: primary electrons bombard the target material and lose energy to the lattice; some electrons make elastic collisions and are emitted with no loss of energy; other electrons make inelastic collisions and are emitted at lower energies while the remainder are brought to rest and become buried (9) within the dielectric. The true secondary electrons, which are originally bound to the solid, gain sufficient energy from the primaries to overcome the work function at the surface. If these secondary electrons were not released the total secondary electron emission coefficient could never exceed one.

Energy Spectrum of Secondaries

Figure 2 shows a typical plot, taken from Harrower (10), of the density of emitted electrons, N(E), as a function of energy where E_o is the energy of the monoenergetic primary beam.

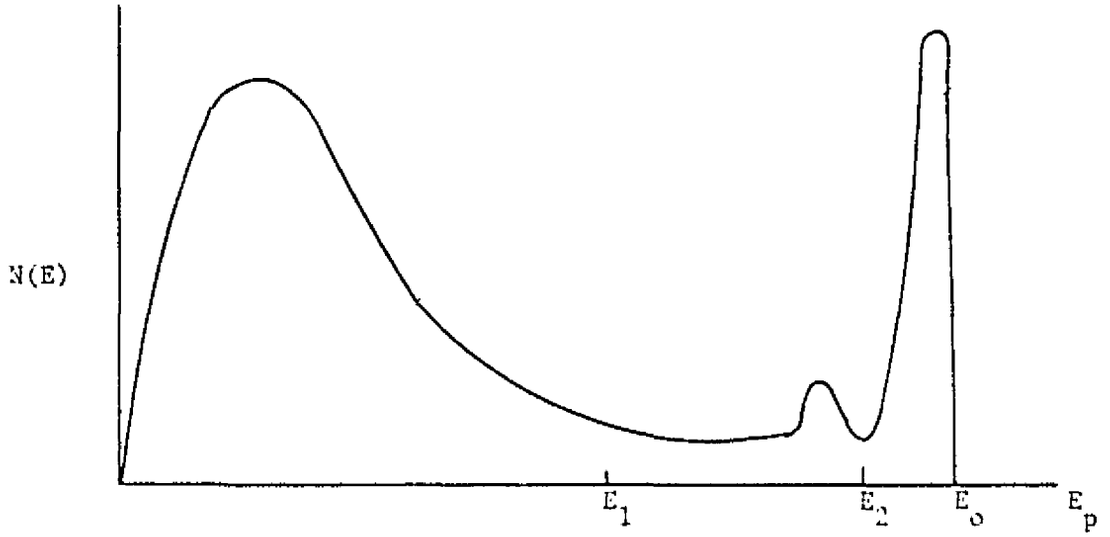

Figure 2. Energy spectrum of secondary electrons.

The first hump in Figure 2 corresponds to the true secondary electrons which possess the lowest kinetic energies. Mathematically the total number of secondaries is

$$\int_0^{E_1} N(E)dE = N_s \tag{1}$$

where $E_{1_{max}}$ is about 50eV (11) for most materials. The inelastically reflected electrons are contained in the energy interval between E_1 and E_2. The number of inelastically reflected primaries is given as the integral of the number density between the values E_2 and E_1.

$$\int_{E_1}^{E_2} N(E)dE = N_i \tag{2}$$

The elastically reflected electrons are bounded to the interval given by E_o and E_2.

$$\int_{E_2}^{E_o} N(E)dE = N_e \tag{3}$$

It should be noted that the total number of primary electrons cannot be deduced by any observations based solely on Figure 2. It is convenient to assign a symbol to the total number of primary electrons which we shall call N_p.

The relative heights of the humps in Figure 2 are not constant as the primary energy is increased. Harrower (10) shows in his article how the three classes of electrons vary in relative strengths as a function of primary energy.

Harrower found for his Molybdenum target that at high primary energies (E_o > 500eV) the true secondaries will dominate the distribution. In the high energy case the last two humps would be missing and only the first hump present. Figure 2 illustrates moderate primary energies (E_o = 50eV - 200eV) where all three classes of emitted electrons may be identified. In the low energies case (E_o = 20eV) it is difficult to distinguish between the three classes of electrons since the elastically and inelastically reflected electrons share the same average energy as the slow secondaries. These observations are supported by L. N. Dobretsov (11) when he states, "The energy spectrum of the true secondaries electrons for metals is practically independent of the primary electron energy beginning at E_o = 18 - 20eV." It should be noted here that our research could not measure N(E), and hence the relative strength of each class, but it is mentioned here for instructive and definitive reasons.

It is useful to express each of the separate emission processes with a different symbol. The total number of emitted electrons is the sum of the three symbols referred to above. If N_p is the primary test charge number and N_i, N_e, and N_s are inelastically, elastically, and slowly emitted electrons, respectively; then we define the three emission coefficients as follows.

$$i = N_i/N_p \tag{4}$$

$$r = N_e/N_p \tag{5}$$

$$\delta = N_s/N_p \tag{6}$$

Each of these coefficients depends differently on such factors as primary beam energy, lattice symmetry, band structure, phonon collisions, and surface cleanliness. An excellent discussion of these interactions is given by L. N. Dobretsov (11). If we define the total secondary electron emission coefficient to be σ then the following equation holds.

$$\sigma = i + r + \delta \tag{7}$$

This and the following paragraph compare results various authors have gathered on elastically and inelastically reflected electron coefficients for some insulators. At high primary beam energies ($E_o > 200eV$) many authors (10, 11, 12, 13, 14) neglect the elastically reflected electrons. I. M. Bronshtien (13) estimates that r is equal to 2-3% for metals and even lower for insulators. S. A. Fridrikhov (12) neglects the quantity r, even at low primary energies, for the mica sample he investigated. Figure 3 plots σ, i, and δ at primary energies up to 50eV for the mica sample. Therefore we will neglect the term r in Equation (7) henceforth.

The role played by the inelastically reflected electrons for mica as a function of primary energies is shown in Figure 3. When an

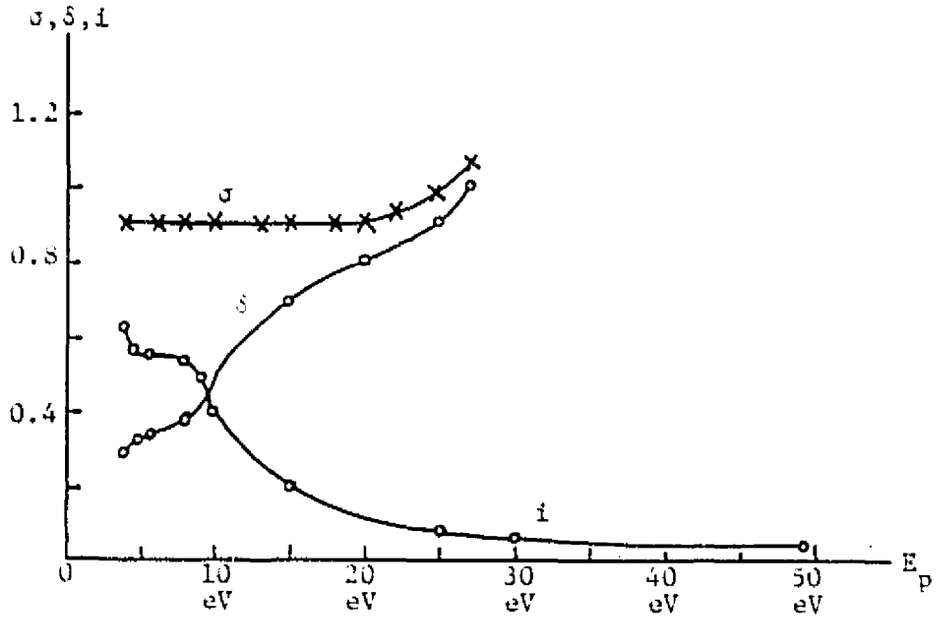

Figure 3. Plot of σ, δ, and i for mica taken from Fridrikhov.

insulator is probed with high primary beam energies, i becomes small compared to δ. Kanter (15) supports this view when he states, "As a result, the correction for the 'backscattered energy' was always less than 5% of the input energy for carbon and less than 8% for aluminum." Since FEP-Teflon is composed mostly of hydrogen, carbon, and fluorine, these figures are of interest. In general materials with a lower effective atomic number have lower inelastically reflected electron coefficients (11). E. G. Martsinovskaya (14) found similar results for the low density polymers he investigated. Because of these results i will be neglected for high primary energies.

Classification of Dielectric Emitters

There are two basic classes of dielectrics as pertains to secondary emission. The first class contains all dielectrics which are relatively poor emitters and where σ_{max} varies from one to four. This class contains such substances as mica, Willermite, polyamide (Kapton), FEP-Teflon, PET (Mylar), CaF_2, LiF, C (Diamond), SiO_2, Al_2O_3, Sb_2S_3, and Si. The second class of dielectrics are those with high emission coefficients on the order of five to fifteen. This class contains such compounds as MgO, BaO, KBr, KI, NaCl, and NaBr. The fact that a substance has lattice symmetry does not seem to be the contributing factor in maximizing σ for dielectrics. MgO and Si both have the same basic lattice symmetry yet the ratio of their respective emissions coefficients is fifteen. Note that no polymers are good emitters but in general σ is smaller for metals and semiconductors than for insulators.

Band Structure in Secondary Emission

The band structure plays an important role in the emission of secondaries from all materials; metals, semiconductors, and insulators. If the energy difference between the conduction band and the valence band ($E_g = E_{cond} - E_{val}$) is greater than the work function of the material, then a secondary near the surface has only to leave the valence band to be free. An electron excited out of the valence will not be stopped by any interactions with electrons in either band. The case just stated applies to insulators of both classes where the better emitters have a smaller bandgap than the weak dielectric emitters. For semiconductors (Si, Ge), where $E_g < E_w$, secondaries must interact with electrons in both bands and this is one reason semiconductors are poor emitters. For metals, potential secondaries lose energy readily through collisions with other conduction electrons.

For insulators the interactions of secondaries with holes, phonons, material defects and trapping centers are the main mechanisms by which secondaries, with sufficient initial kinetic energy to leave the material, are stopped and not emitted. The recombination of holes and secondary electrons is very unlikely and will be ignored. A collision with a phonon can only cause a small loss of energy. Though a collision with an optical phonon causes only a small change in momentum, a collision with an acoustical phonon can provide large changes in momentum which can scatter the secondary or change its direction relative to the surface. Repeated collisions with phonons can slow a secondary down yet the main stopping mechanism for secondaries is their interactions with trapping centers and material defects.

Dobretsov (11) states, "The capture of an internal secondary by a defect is a decisive factor in the secondary emission from substances with a large number of defects." It is very likely that for polymer dielectrics like FEP-Teflon, where there is little lattice symmetry, there is an abundance of dangling bonds and trapping centers.

The emission of secondary electrons from an insulator being stimulated by a primary electron beam is a complex process. Important factors which contribute to emission mechanics are the material band structure, lattice defects, material work function, electron-phonon interactions, and electron transition probabilities. Also secondary emission can be influenced by experimental procedures which affect surface contamination or surface roughness.

Quantitative Theory of Secondary Emission

It is helpful to start with a simple theory and modify it as necessity demands. Many authors (11, 16, 17, 18, 19, 20, 21, 22, 23) use the following model and theory to characterize secondary emission from a dielectric. The empirical model is semiquantitative at best, yet it nevertheless is quite useful. It should be emphasized that the following model does not describe the behavior of elastically or inelastically reflected electrons. This fact will be emphasized by using the symbol δ in all equations using this model. Later in this paper under the proper assumptions δ will be replaced by σ but until then we will use δ.

We assume the true secondary electron emission coefficient will be given as

$$\delta = \int_0^R n(x,E_o) f(x) dx \tag{8}$$

where $n(x,E_o)dx$ represents the average number of secondaries produced by one primary at depth x and layer thickness dx below the surface. Figure 4 shows the one-dimensional geometry being considered by this model where R is the maximum depth to which any given primary electron can penetrate for a fixed initial energy, E_o.

L. N. Dobretsov (11) refers to $n(x,E_o)$ as the excitation density for secondary electrons. Regardless of the name $n(x,E_o)$ has the units of number of secondary electrons (per primary) per unit length. The function f(x) is the probability that a secondary electron will be emitted from the material for any x. All authors assume that the probability function associated with the release of secondaries from a dielectric is a function which decreases exponentially with increasing x. The standard form of f(x) for normally incident electrons is

$$f(x) = f(0)\exp(-x/X_s) \tag{9}$$

where f(0) represents the probability of escape right at the surface. The quantity X_s is a measure of the ability for a secondary electron to leave the material. X_s has the units of length and varies between 20Å and 50Å for most materials. As we would expect the probability function must go to zero as x approaches infinity.

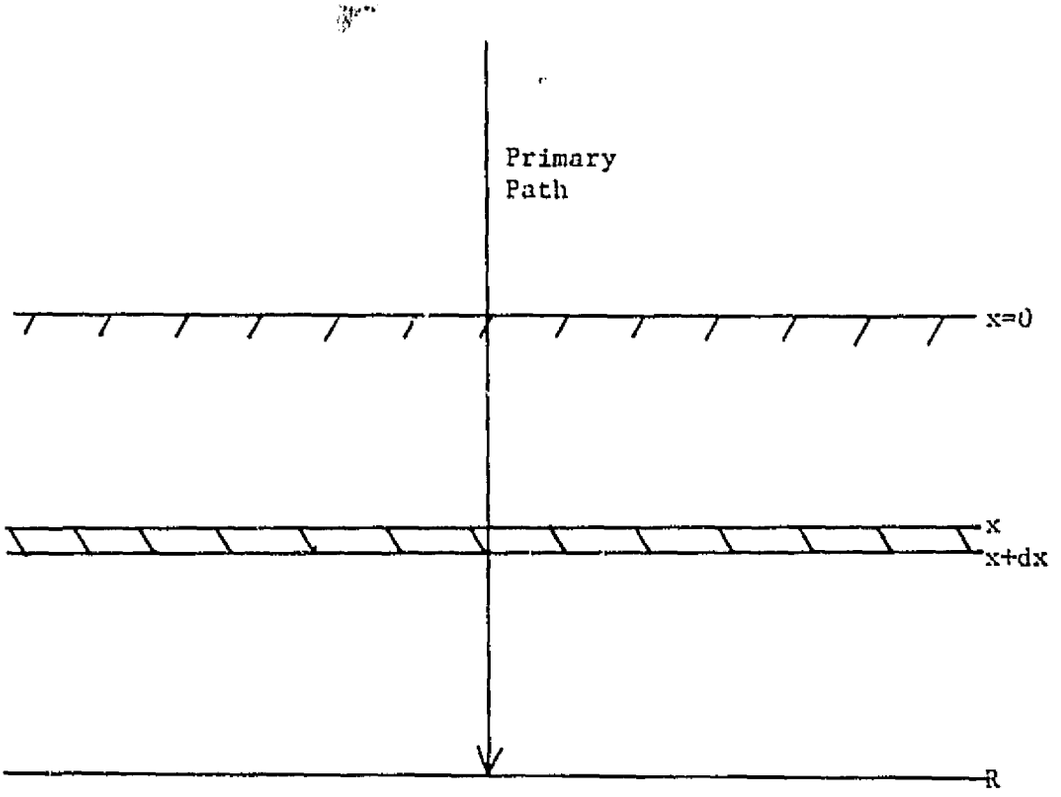

Figure 4. One-dimensional analysis of secondary emission.

Description of Mathematical Terms

The meaning of the quantities R, X_s, $\bar{f}$, $\bar{x}$, $\bar{\bar{x}}$, and l_c will be revealed in this subsection. The statistical quantities $\bar{f}$, $\bar{x}$, and $\bar{\bar{x}}$, as described by Dobretsov (11), provide a useful tool for gaining insight into complex mathematical expressions.

The maximum depth to which any primary electron can penetrate is a constant, with respect to x, at a fixed primary energy and is defined to be R. The range R is assumed to be functionally dependent only on the impact energy E_o.

The physical meaning of X_s is revealed in the following paragraph. Let us suppose secondary electrons are generated at point "o" as shown in Figure 5. We assume here that the secondary electrons will be scattered isotropically so that only a small number of them will be pointed straight back at the surface. We also assume as did Jonker (21) that "The secondaries are absorbed in the material according to the exponential apsorption law." Therefore, as the secondaries travel through the dielectric the probability that they have not become trapped decreases exponentially. What Equation (9) states is that the probability of escape through the surface is also an exponential where X_s is secondary range and f(0) is the probability that an electron may leave the surface at the plane x=0.

If we define a quantity l_c to be the free mean path of a secondary electron prior to being retrapped in another trap center, it should be clear that X_s is less than l_c. In a strict mathematical sense the surface loss function, which may be derived from the bulk

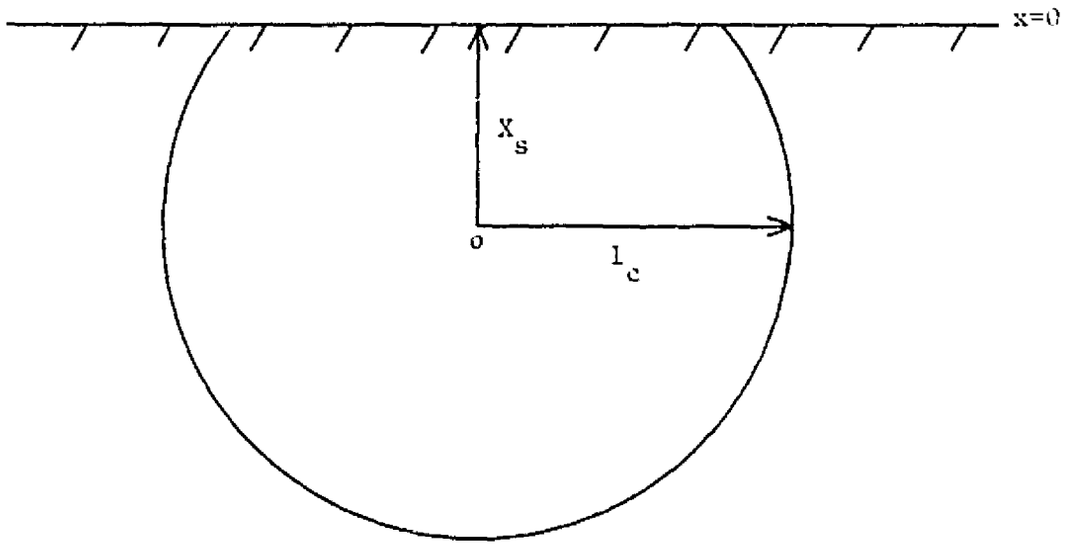

Figure 5. Secondary range and free mean path.

function, cannot be a simple exponential function. The surface loss function was derived for the case of isotropic generation of secondaries at an arbitrary distance x where the probability that a secondary is absorbed (trapped) is proportional to $\exp(-x/l_c)$. It is sufficient to state here that there are other terms resulting from the integration which must be ignored if one is to model the surface loss function as a simple exponential as most authors do (11, 16, 17, 18, 19, 23).

Dekker (24) suggests a theory where if the primary range R is greater than the secondary range X_s then the production of secondaries per unit depth $n(x,E_o)$ may be taken to be a constant. This theory depends on a high trap density and leads to a model which states that the probability of trapping secondaries is proportional to $\exp(-x/L)$ where L is equal to the diffusion length of the secondaries. This theory uses the standard diffusion law equations and assumptions in modeling the escape of secondaries for the insulator. These observations provide insight into the nature of Equation (9).

The depth to which the primary electrons penetrate the surface increases with increasing primary beam energy. The average depth at which internally generated secondary electrons are created is

$$\bar{x} = \frac{\int_0^R x n(x,E_o)\,dx}{\int_0^R n(x,E_o)\,dx} \tag{10}$$

where E_o is the initial primary electron energy and is taken to be a constant for each integration. As the primary electron energy is increased $\bar{x}$ increases but the secondaries mean escape probability, $\bar{f}$, will decrease.

$$\bar{f} = \frac{\int_0^R xf(x)n(x,E_o)dx}{\int_0^R n(x,E_o)dx} \tag{11}$$

The mean escape probability $\bar{f}(R)$ will give the probability of escape for secondaries as a function of the primary range, where the primary range is a function only of the fixed initial primary energy

The mean electron escape depth $\bar{\bar{x}}$ as is given by Equation (12) represents the depth at which secondary emission is most probable for a given primary energy.

$$\bar{\bar{x}} = \frac{\int_0^R xf(x)n(x,E_o)dx}{\int_0^R f(x)n(x,E_o)dx} \tag{12}$$

The significant difference between $\bar{x}$ and $\bar{\bar{x}}$ is that $\bar{\bar{x}}$ has been weighted by the secondary electron probability function whereas $\bar{x}$ depends only on the excitation density.

Example of Statistical Quantities

An example will illustrate the various roles played by the terms defined in the previous subsection.

In our example we will use f(x) as stated and assume that the excitation density is a constant over the region from x=0 to x=R. This assumption is discussed in further detail later and the results are stated below.

$$\bar{x} = R/2 \tag{13}$$

$$\bar{\bar{x}} = \frac{X_s(1-\exp(-R/X_s)(R/X_s+1))}{(1-\exp(-R/X_s))} \tag{14}$$

$$\bar{f} = (X_s/R)f(0)(1-\exp(-R/X_s)) \tag{15}$$

At low primary energies when R is small, compared to X_s, $\bar{\bar{x}}$ reduces to R. This is accomplished by setting exp(y) = 1+y in Equation (14). A similar expansion of the exponential term reveals that $\bar{f} = f(0)$ which states that at low primary energies the probability of escape is at its maximum. At high primary beam energies when R is much greater than X_s the escape probability $\bar{f}$ drops off rapidly as is indicated by the exponential behavior of Equation (15). When $R >> X_s$, $\bar{\bar{x}}$ will be equal to X_s and the ratio $\bar{x}/\bar{\bar{x}}$ will be equal to $R/2X_s$. When this ratio is near one, under any assumptions, the secondary emission will be very close to a maximum. The quantity R/X_s as defined herein is an important physical parameter we will refer to frequently in the discussions to follow.

Assumptions Used to Model Emission

Continuing with the development of our model for δ, it is necessary to state the approximations which justify the use of Equation (8). Four initial assumptions are as follows: (1) the primaries move in straight trajectories through the dielectric along the direction of incidence perpendicular to the surface, (2) the primary energy loss per unit path length is given by Whiddington's Law

$$\frac{dE(x)}{dx} = \frac{-A}{E(x)} \tag{16}$$

where A is a constant characteristic of each material and E(x) is the amount of energy a primary has as it penetrates the surface, (3) the number of secondaries produced in a layer of dx by a single primary is proportional to dE(x)/dx, i.e.,

$$n(x,E_o) = -K_1\frac{dE(x)}{dx} \tag{17}$$

where $1/K_1$ represents the average excitation energy required to produce a secondary, (4) finally, it is assumed that the probability that a secondary produced at a depth x can escape from the surface is given by the exponential absorption law $f(x) = f(0)\exp(-x/X_s)$.

If E_o is the energy which the primary electrons have as they strike the surface, then the primary energy as a function of x (the distance measured perpendicular into the surface) is given as

$$E^2(x) = E_o^2 - 2Ax \tag{18}$$

which follows from integration of Equation (16) from x=0 to some arbitrary distance x. The approximate maximum depth of penetration of the primaries becomes

$$R = E_o^2/2A \ . \tag{19}$$

If we substitute Equations (16) and (18) into Equation (17) we find

$$\sqrt{A}\ K_1(2R-2x)^{-1/2} = n(x,E_o) = \sqrt{\frac{A}{2}}\ K_1(R-x)^{-1/2} \tag{20}$$

The density of electrons $n(x,E_o)$ is a maximum when the primary electrons reach the end of their path. As a matter of fact, Equation (20) tends to infinity as x approaches R (note the integral is still finite due to the damping action of the exponential in the integrand). It is important to the analysis used later in this report to determine how δ behaves as a function of high probe energies. When the primary range R is much greater than the secondary range X_s, Equation (20) may be approximated as

$$n(x,E_o) = n(0,E_o) = \frac{AK_1}{E_o} \tag{21}$$

because within the integration of Equation (8) there is very little contribution to the integral from $n(x,E_o)f(x)$ for $x >> X_s$ due to the action of the exponential probability function. Hence δ is given as

$$\delta = \int_0^R n(0,E_o)f(x)dx$$

$$\delta = \int_0^R \frac{AK_1}{E_o} f(0)\exp(-x/X_s)dx =$$

$$\frac{f(0)X_s AK_1}{E_o}\,(1-\exp(-RX_s)$$

$$\delta = \frac{C_1}{E_o}\left[(1 - \exp(-R/X_s)\right]$$

$$\delta \simeq \frac{C_1}{E_o} \tag{22}$$

where $\exp(-R/X_s) \simeq 0$ for $R >> X_s$ as we assumed originally.

Power Law Model of Emission

The reader should note that we have derived a simple result based on rather simple assumptions. Recent authors (16, 17, 18) who have published papers on secondary emission have found, however, that this model does not predict correctly the behavior of all materials. A more general expression for δ is given below as

$$\delta = (E_c/E_o)^n \tag{23}$$

where n is some rational number and E_c is the critical voltage at which $\delta = 1$ for various materials. Lye and Dekker (16) present another model called the power law theory which predicts the experimental behavior of δ more precisely in the region of high probe energies. This correction is necessary for insulators and good for most

materials. Whiddington's law is modified by introducing a generalized exponent (a constant for a specific material) in the primary beam energy. Equation (16) is now replaced by Equation (24) stated below.

$$dE/dx = -A/E^{n}(x) \tag{24}$$

Integration of Equation (24) is displayed in Equation (25) where the upper limits E and x are free running variables. E is the energy the primary has left at an arbitrary distance x within the dielectric.

$$\int_{E_o}^{E} E^{n}(x)\,dE = \int_{0}^{x} -A\,dx \tag{25}$$

The primary beam energy, as a function of depth, is given by the left hand side of Equation (26) which follows from Equation (25).

$$E^{n+1}(x) = E_o^{\,n+1} - A(n+1)x \tag{26}$$

Setting the left hand side of Equation (26) equal to zero and solving for the primary range R, we find

$$R = \frac{E_o^{\,n+1}}{A(n+1)} \tag{27}$$

which is similar to Equation (19) stated earlier.

An integration similar to that carried out in Equation (20) reveals that at high primary energies δ varies as E_o^{-n}, as stated in Equation (23).

The previous case, called the power law theory, which is based on an excitation density similar to the one shown in Equation (20), can

be modified further in light of experimental results (25, 26). The following model assumes $n(x,E_o)$ to be constant as is done by Katz, et al. (1) in one of the models used in satellite design simulations.

Straggle Theory of Secondary Electron Emission

The following theory has been presented by Lye and Dekker (16) and is called the straggle theory. The main assumption of this theory is that the excitation density $n(x,E_o)$ is a constant up to a point R, where R is given by Equation (28)

$$R = K_2 E_o^{n+1} \tag{28}$$

where K_2 and n are constants for various materials. The model is based on the experimental results of Young (25, 26) and Kanter (15) which suggest that for primary energies from 2.5keV to 10keV the excitation density $n(x,E_o)$ is constant. This is equivalent to stating that the primary energy loss rate dE/dx is constant. Figure 6 shows Young's results where he has plotted fraction of energy dissipated versus the fraction of range covered for Al_2O_3.

The derivative of the straight line shown is a constant and these authors (16, 25, 26) argue that this implies $n(x,E_o)$ is therefore a constant. The basic concept involved is that the number of primary electrons in a beam of fixed initial kinetic energy decreases linearly with distance into the surface and becomes zero at the primary range R. The probability that a primary electron will pass through a solid layer is given by

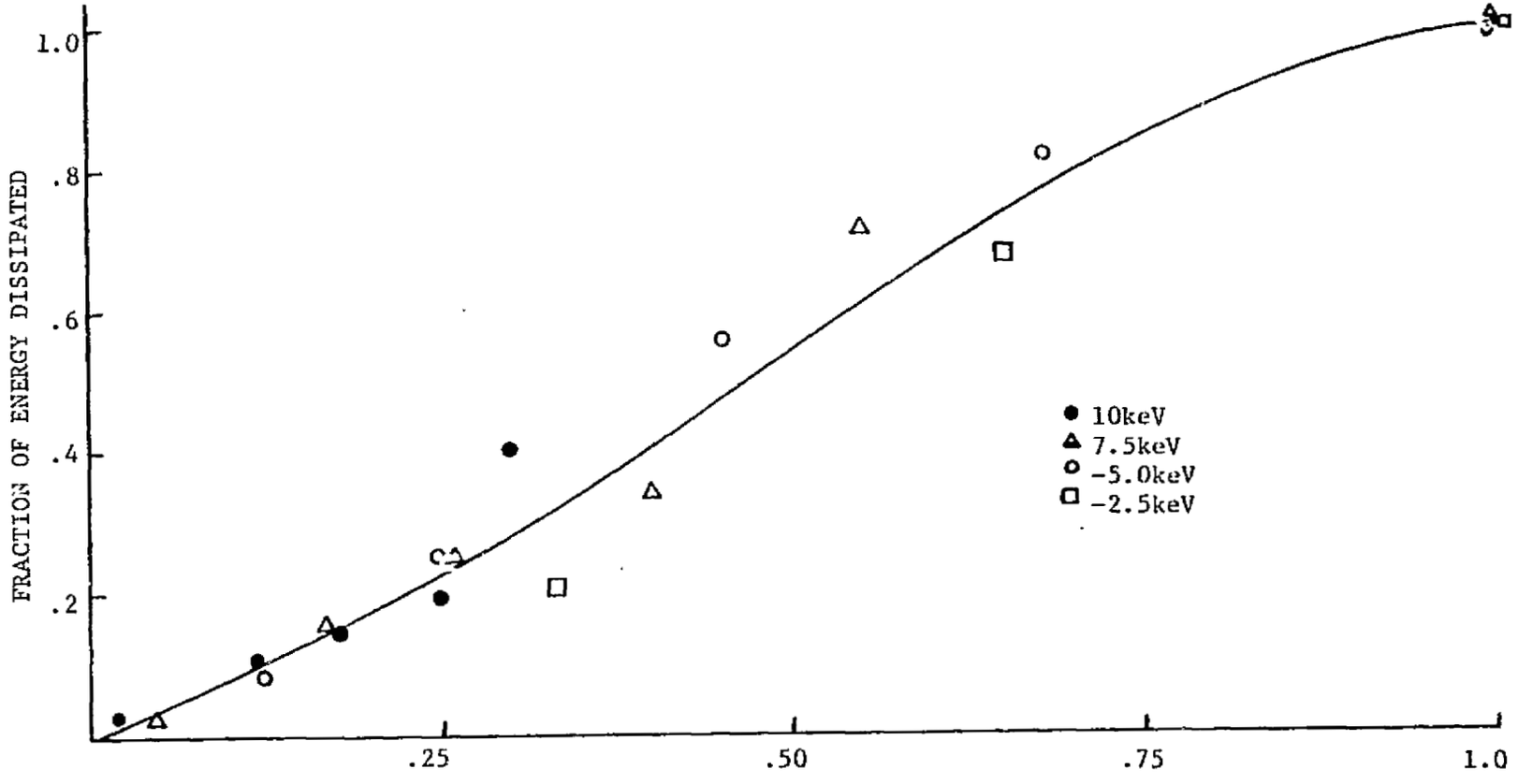

Figure 6. Fraction of energy dissipated versus fraction of range covered for Al_2O_3 taken from Young.

$$p(x,E_o) = 1 - x/R \tag{29}$$

and defined to be zero for $x > R$. In the power law theory the probability that a primary would pass through a solid layer was constant since electrons traveled the entire distance R. Figure 7 shows the number of primary electrons (N_o) left within the initial pulse after traveling a distance x into the dielectric for each theory.

The probability functions p(x) and f(x) are not the same since they describe different processes. The function f(x) models the absorption of secondaries on their way to the surface while p(x) is the probability that a primary electron has been stopped at a particular value of x. It is assumed in both theories that the probability that a primary electron has been stopped is proportional to the probability that a secondary has been generated. Therefore if the primary beam is losing a constant amount of energy (electrons) as a function of distance x, then a constant amount of generated secondaries per layer dx is implied.

Figure 8 shows the comparison of $n(x,E_o)$ as defined by Equation (21) in the "power law" case and by Equation (30) written below.

$$n(x,E_o) = \frac{K_1 E_o}{R} = \frac{K_1}{K_2 E_o^n} \tag{30}$$

Equation (30) is similar in form to Equation (21) since both of these quantities are constants with respect to x, the variable of integration.

Once again we integrate Equation (8) using Equation (30) and the same probability function as before. Since $R = K_2 E_o^{n+1}$, this is written as

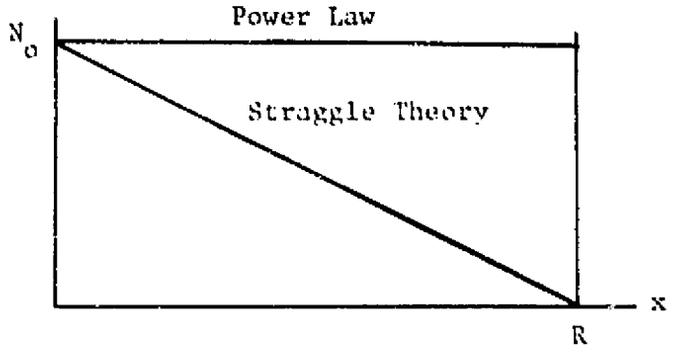

Figure 7. Number of electrons remaining in the initial primary beam.

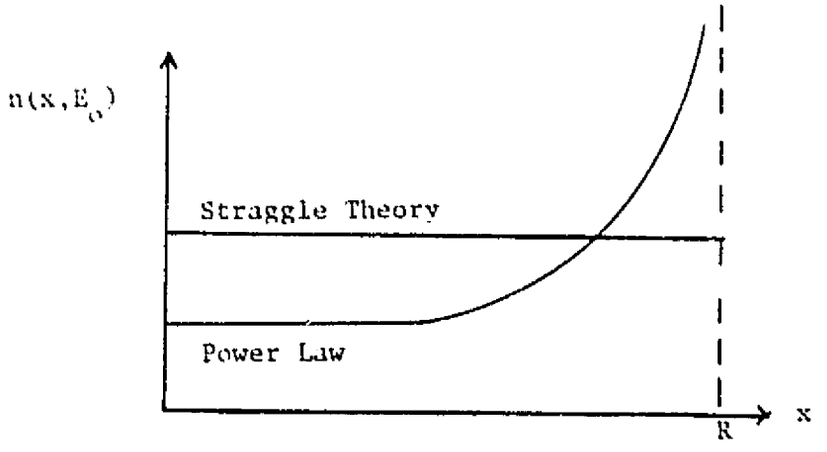

Figure 8. Excitation density as a function of depth for the straggle and power law theories.

$$\delta = \int_0^R \frac{K_1 E_o}{R} f(0)\exp(-x/X_s)dx =$$

$$f(0)\ \frac{K_1 E_o X_s}{R}\left[1 - \exp(-R/X_s)\right] \qquad (31)$$

The difference between Equation (31) and (22) is that here we don't force the ratio R/X_s to be large as we did in the derivation of Equation (22). For Equation (21), $n(x,E_o)$ was allowed to be constant only if R/X_s was large. In the straggle theory the exponential is kept so that this assumption applies to the full range of x and R. If $R = K_2 E_o^{n+1}$ then Equation (31) may be rewritten as

$$\delta = f(0)K_1 E_o \frac{\left[1 - \exp(-K_2 E_o^{n+1}/X_s)\right]}{(K_2 E_o^{n+1}/X_s)} .$$

This equation applies to the full range of impact energies (E_o) where Equation (22) was only good for high (2keV) primary energies. It should be noted however, that Equation (31) reduces to Equation (23) for high primary energies. It is curious that Lye and Dekker (16) used Young's experimental results (25, 26) for high energy primaries and applied them to the low energy case also, in spite of no experimental basis. Nevertheless, others (1) have assumed the same thing with no justification.

Emission Theory for Obliquely Incident Electrons

We are now ready to extend this discussion a little further and look at how Katz, et al. (1) modified these theories to suit the needs

of the NASCAP program. The authors essentially changed the probability function (9) and introduced a cos(θ) term in the argument of the exponential.

$$f(x) = f(0)\ \exp(-x\cos(\theta)/X_s) \tag{32}$$

Figure 9 shows the geometry used in modeling Equation (32).

If one assumes that it is the normal component of the electron depth that should be used for the probability exponentials argument, then Equation (32) is the logical choice. Two references, Jonker (21) and Bruining (19) have done calculations which state that

$$E_{max}(\theta) = \frac{0.71}{(\cos(\theta)/X_s A)^{1/2}} \tag{33}$$

where A is defined in Equation (24). Even for the straggle theory where Equation (24) is replaced by Equation (34), we have

$$\frac{dE(x)}{dx} = -\frac{E_o}{R(E_o)} = \frac{-1}{K_2 E_o^n} \tag{34}$$

where $(n+1)A = K_2^{-1}$ and Equation (33) is still valid.

Equation (35) expresses the ratio of two separate energy maximums measured at two separate angles.

$$\frac{E_{max}(\theta_1)}{E_{max}(\theta_2)} = (\cos(\theta_2)/\cos(\theta_1))^{1/2} \tag{35}$$

This equation will be referred to later when our data is compared to theoretical predictions.

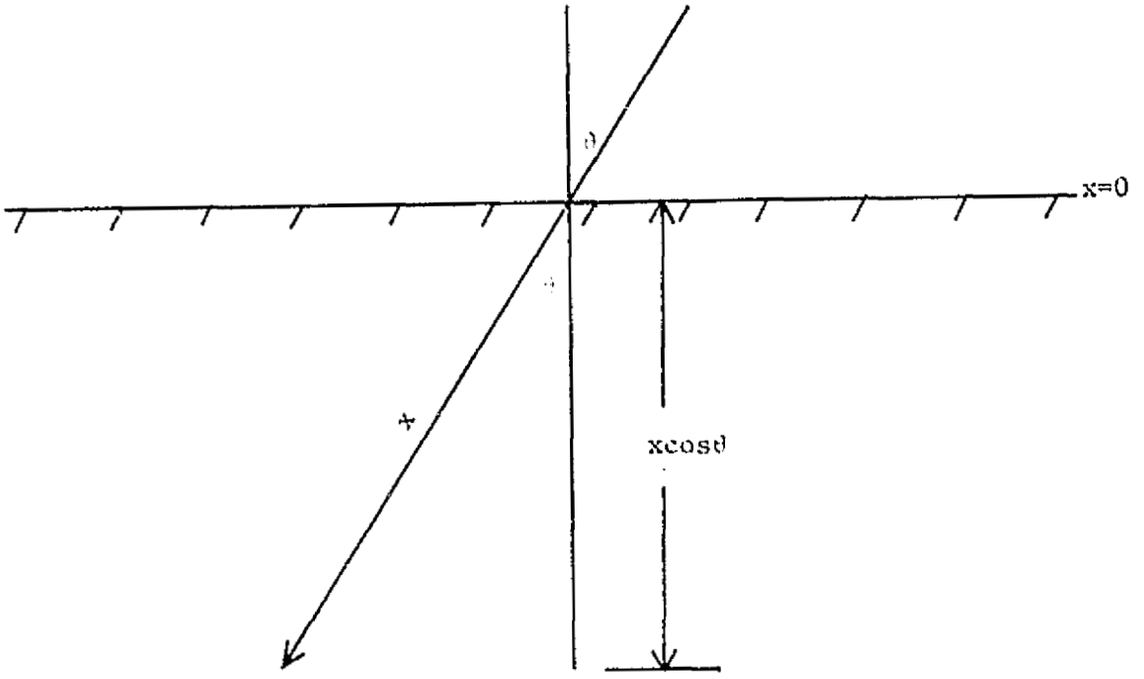

Figure 9. Geometry used to model oblique incidence.

Katz, et al. (1) integrate Equation (8) in their own form where

$$\delta = C_2 \int_0^R \left|\frac{dE}{dx}\right| \exp(-x\cos(\theta)/X_s)dx \tag{36}$$

and where Equation (32) is the probability function used before (19, 21). The result of this integration where $|dE/dx|$ is taken as a constant is

$$\delta = X_s C_2 \left|\frac{dE}{dx}\right| \frac{[1 - \exp(-R\cos(\theta)/X_s)]}{\cos(\theta)} =$$

$$X_s C_2 \left|\frac{dE}{dx}\right| \frac{[1 - \exp(-R\cos\theta/X_s)]}{\cos(\theta)} =$$

$$C_3 \frac{[1 - \exp(-Q)]}{\cos(\theta)} \tag{37}$$

where $Q = R\cos(\theta)/X_s$ and $C_3 = (C_2 X_s)\ |dE/dx|$. This predicts that at high primary energies where $Q >> 1$, the secondary electron emission coefficient will vary as a function of θ as a constant times $\sec(\theta)$.

Katz, et al. (1) make one last modification of the integral expressed by Equation (36) and this is to estimate dE/dx as the first two terms in a Taylor series.

$$\frac{dE}{dx} = a_0 + a_1 x \tag{38}$$

No other referenced authors used this model, but they justify the usage of Equation (38) based on energy range data presented in their text. This model estimated the primary range as before where $R = K_2 E_o^{n+1}$.

Integration of Equation (36) under these assumptions yields the result stated below

$$\delta(E_o,\theta) = C_2 R a_o \frac{[1 - \exp(-Q)]}{Q} + C_2 R^2 a_1 \frac{[1 - (Q+1)\exp(-Q)]}{Q^2} \quad (39)$$

where $Q = R\cos(\theta)/X_s$ and $R = K_2 E_o^{n+1}$. For high primary energies the second term in Equation (39) becomes negligible. Therefore for high primary energies the ratio of δ for two separate angles reduces to

$$\frac{\delta(\theta_1)}{\delta(\theta_2)} = \frac{\cos(\theta_2)}{\cos(\theta_1)} \quad (40)$$

The equations stated in this first chapter will be referenced in Chapters IV and V where data and theories are compared.

Summary

The important features of Chapter I are that mathematical models, as developed in the literature, have been presented so that they will be available for comparing theory and experiment. The assumptions involved in the mathematical models have been reviewed as they pertain to polymers.

The important equations to keep in mind are Equations (23), (37), and (40). Equation (23) will be used in Chapter IV in order to help estimate the primary beam charge. Equation (39) reduces to Equation (37) for high primary energies (E_o = 1keV) because Q is proportional to energy and the second term varies as Q^{-2}. Equation (40) is a further simplification of Equation (39) where exp(-Q) has been approximated as zero.

The term exp(-Q) was estimated to be negligible for FEP-Teflon over the range of angles investigated herein and therefore the importance of the term is not stressed here. If K_2 = 350 Å/keV as is indicated by

Katz, et al. (1) for TFE-Teflon then for primary energies of 1keV the ratio of R/X_s will be about seven and the exponential term will be three percent at $\theta = 70°$. At 2keV R/X_s will be 21 and the exponential term will be equal to three percent at $\theta = 80°$. The angular limit of the experimental data is about 70°, therefore the effects of the exponential term on data taken in the range $1keV \lesssim E_o \lesssim 10keV$ were not noticed.

CHAPTER II

EXPERIMENTAL APPARATUS

Two separate experimental procedures were followed in the collection of data. Firstly, the potential field distribution within the electrostatic environment was obtained from measured electron trajectories. From knowledge of the field distributions it was possible to conduct a second set of experiments where the primary beam impacted the dielectric surface at specified angles of inclination. A description of the apparatus used in each procedure is given below.

It was necessary to design and fabricate the entire apparatus using few prefabricated parts. Each subsystem--probe gun, flood gun, signal monitoring equipment, motor drive mechanisms, deflection circuitry--had to be working as a separate part before any unified experiments could be accomplished. The malfunction of any part could render an experiment inconclusive.

The basic experimental system, as described in previous reports, (5, 8) is shown in Figure 10. The dielectric sample is contained within a grounded half-cylindrical shell. The sample is mounted on a flat stainless steel platform and it is covered with a 5-mil sheet of stainless steel shim stock. A rectangular opening in this cover defines the area of the specimen to be tested. A separate dielectric sheet isolates the metalized backside of the FEP sample from the grounded platform. A wire, which connects the specimen to the electrical monitoring equipment, is attached to the specimen backside with silver-laced epoxy.

The electron probe gun and flood gun are firmly mounted to the vacuum chamber floor and are unable to move. However, the platform may

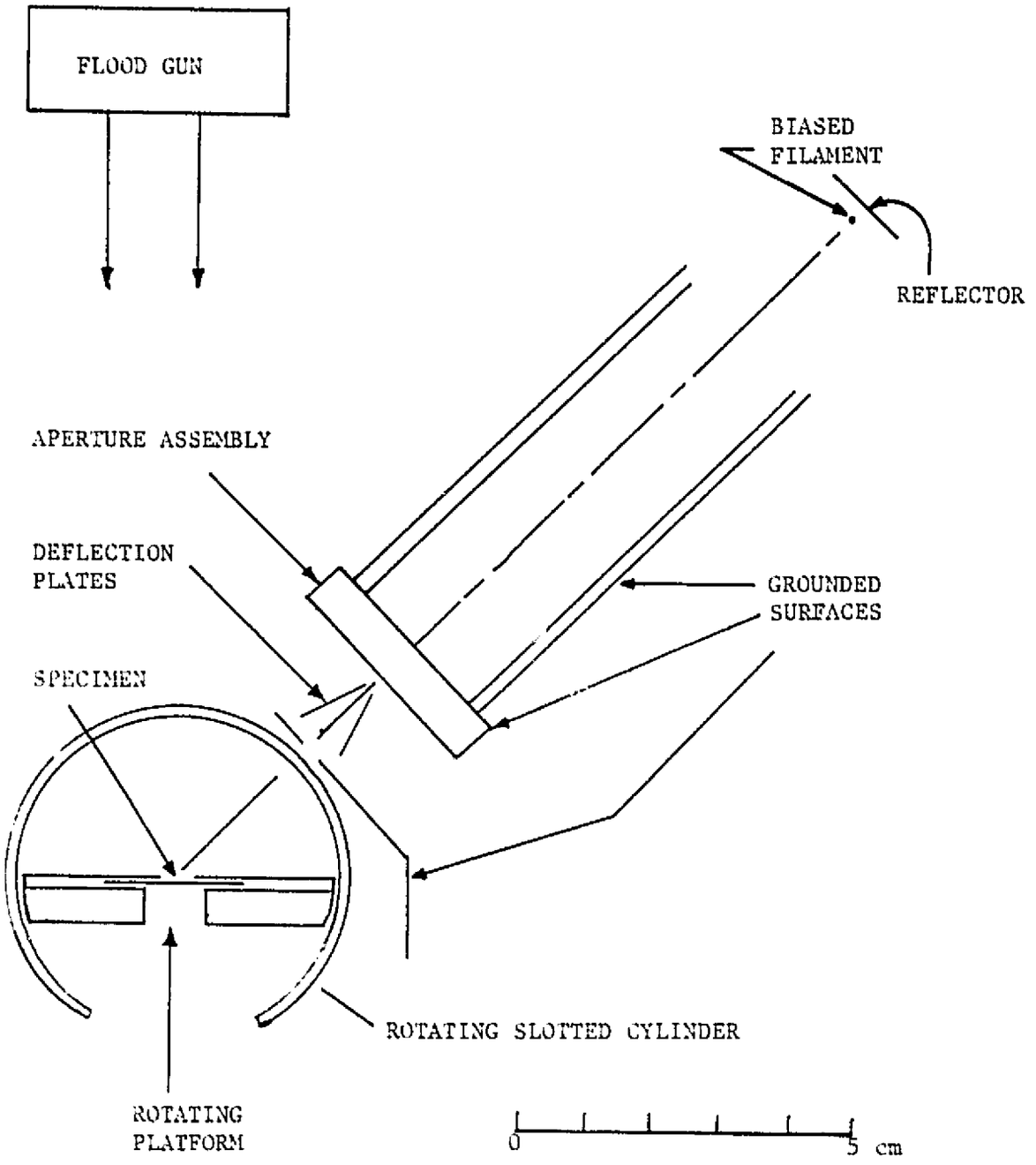

Figure 10. The specimen, the chamber where it is mounted, and the two electron sources used for charging and probing the specimen.

be rotated so that the specimen surface may be exposed to either gun at normal or non-normal incidence.

Vacuum System

All system measurements were made within a 45-cm diameter stainless steel bell jar which is evacuated by a turbomolecular pump, and at a pressure below 10^{-6} torr--the lower limit of the gauge which was used. The vacuum system was run continuously day and night, and it was also "baked out" by leaving red hot tungsten filaments on at all times which aided in outgassing of surfaces. All metals placed in the system were cleaned with trichlorethelene first, methanol second, and lastly acetone, and were then baked under a heat lamp to aid in outgassing. The pump was able to reach 10^{-6} torr within one hour after being at room pressure, yet reproducible results were not attained until the system had been in a vacuum for a few days.

Motor Drives

The cylinder and mounting platform are turned with stepper motors which have 200 steps per revolution. These motors are located outside the vacuum system. They turn shafts which pass through vacuum seals, and the shafts in turn are coupled to the cylinder and platform through spring-tensioned wires stretched over pulleys. This mechanical arrangement provides precise, repeatable positioning of both cylinder and platform. The motors themselves are driven from an 11 volt source through a control system which allows single-step operation or sequen-

tial stepping at four steps/sec in either direction. Decade counters and 7-segment displays monitor the stepping sequences.

The platform and cylinder may be rotated independently from one another. Thus the platform may be oriented so that the probing beam approaches the specimen from any angle. Then the cylinder, which carries the beam detector, may be rotated so that the beam exit position can be determined. As the necessary rotations are being made, the specimen remains in a controlled electrostatic environment. The beam may fall between discrete positions available to the detector and if this happens, a change of voltage on the beam deflection plates can provide the slight adjustment needed to center the beam on the detector. The detector on the periphery of the cylinder moves 0.8 mm/step on the average with some observed differences in step sizes being attributed to the motor tolerances.

Flood Gun

Mono-energetic electrons drawn from a heated tungsten wire can be accelerated toward the specimen in a broad beam. This technique has been used before and it has provided more than adequate current density to the specimen surface, charging it in a few seconds to potentials as high as 20kV. A special feature of this system is that the specimen can be tilted relative to the beam direction such that skewed charge distributions become possible.

Charging is done when the rotating cylinder has its window between the flood gun and the specimen. This allows the specimen to be

charged so that after the cylinder is rotated back to the original position, the specimen is contained within a controlled electrostatic environment.

Charging of the dielectric surface is accomplished by first biasing the flood gun assembly at some negative potential and then increasing the tungsten filament current from 0 to 5 A for a few seconds. Accumulated charge is monitored with an electrometer so that the operator will know when the charging has stopped. The current through the filament is then returned to zero, and lastly the flood gun assembly is returned to ground potential. In this procedure the emitting filament must be turned off before the high voltage bias is.

Discharging of the dielectric calls for a reversal in the order just stated. When the surface is being discharged, the high voltage bias is slowly (500V/s) turned down to zero. Next the filament current is returned to zero. By turning the high voltage power supply down slowly the flood beam potential is kept between the unity points on the secondary emission curve and the specimen loses charge. If the high voltage is turned down too quickly, total discharging might not occur.

Cycling of the dielectric from charging to discharging and back again can create dipole layers of charge within the dielectric. A paper written by Beers, et al. (9) models the effect of buried layers within FEP-Teflon and they found that, within the region where most secondaries are released, the electric field created by deeply buried primary electrons is small and independent of charging history. Therefore, the effects on secondary emission caused by internal electric fields generated through discharging and charging of the dielectric are ignored.

It is useful to note that only those electrons right on the surface of the dielectric (within 50 Å) can be liberated during the discharging process. In one cycle, equal amounts of charge are put onto the surface and removed, such that after one cycle the dielectric as a whole is uncharged. Yet there is a positive layer of charge on the surface and a negative buried layer in the substrate.

Another aspect of the charging system that is worth mentioning is that an uncharged specimen could be charged by rotating the platform from a position parallel to the flux of electrons to a position where it was perpendicular to the electron flux. This procedure allows the specimen to be charged by a non-normal flux of electrons and it also allows one to detect whether or not the pulley wires had become broken or disengaged.

Collimated Electron Beam

The desired attributes of the probing beam are that it be monoenergetic, deflectable, and shaped like a ribbon having dimensions of 0.15 mm x 1 mm. The electrons are drawn from a heated tungsten filament and are sufficiently monoenergetic as long as the accelerating potential has low ripple. Deflection is easily accomplished with the biased plates shown in Figure 10. The shaping is a more critical problem which is approached in this work by allowing the electrons to stream through collimating slits. This is feasible since electrostatic defocusing is not significant at the low operating current of 1 nA.

It was necessary to bend the probing beam with deflection plates as shown in Figure 10. By rotating the specimen platform and adjusting

the deflection plate voltage it was possible to inject the primary beam into the hemi-cylinder with various angular attacks. Figure 11 shows two angles, α and β, where α is referred to as the angle of cylindrical incidence and β is referred to as the primary angle of inclination. A third angle θ is defined which is the angle of incidence the primary electron has just prior to surface impact. In general, α is never equal to θ for charged specimens.

Angle α could be varied from 0° to 180° while angle β could be adjusted about 20°. Appendix A provides the details concerning how the deflection factor, D, was found for various primary beam energies. Deflection factor D has the units of radians per volt, and when multiplied by a deflection voltage yields β, the angle of interest. One further angle is defined as γ, which is the angle that a reflected primary beam has with respect to the specimen platform. Figure 12 shows a typical reflected electron trajectory for normal incidence (α = 90°) upon a charged specimen where β is practically in the range of 1-50 milliradians.

It was possible to measure the probe beam thickness, at the cylinder entry point (up front), by deflecting the beam onto two discrete detector positions separated by one step (1.8° or 0.8 mm). The difference in deflection voltages between the two discrete detector positions is a measured quantity V_{dv}. A plot of the probe beam current as a function of deflection voltage is shown in Figure 13 for two discrete detector positions. The difference in deflection voltage (V_{dv}) is given as ($V_1 - V_2$).

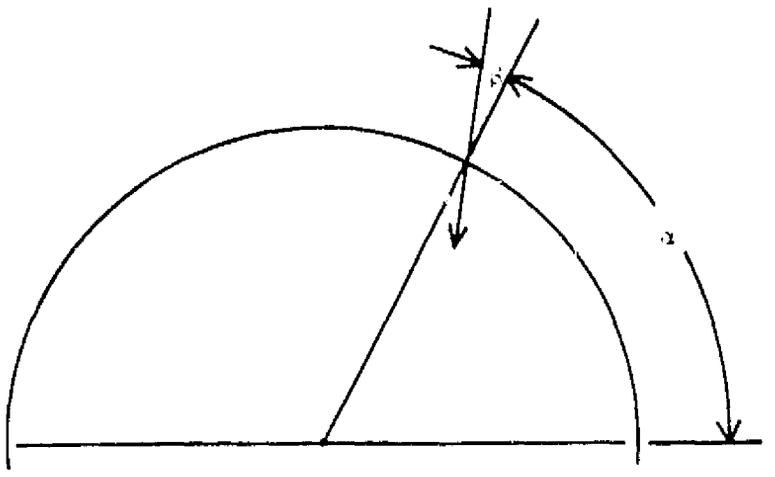

Figure 11. Angle of cylindrical incidence α and angle of inclination δ.

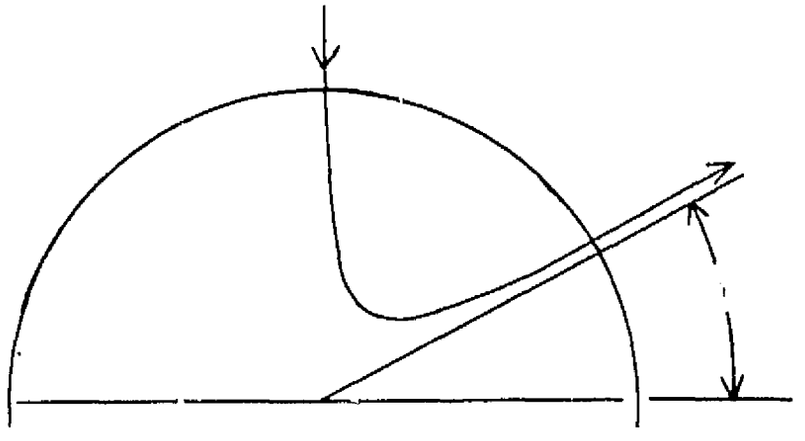

Figure 12. Plot of a typical reflected trajectory where the exit angle γ is shown.

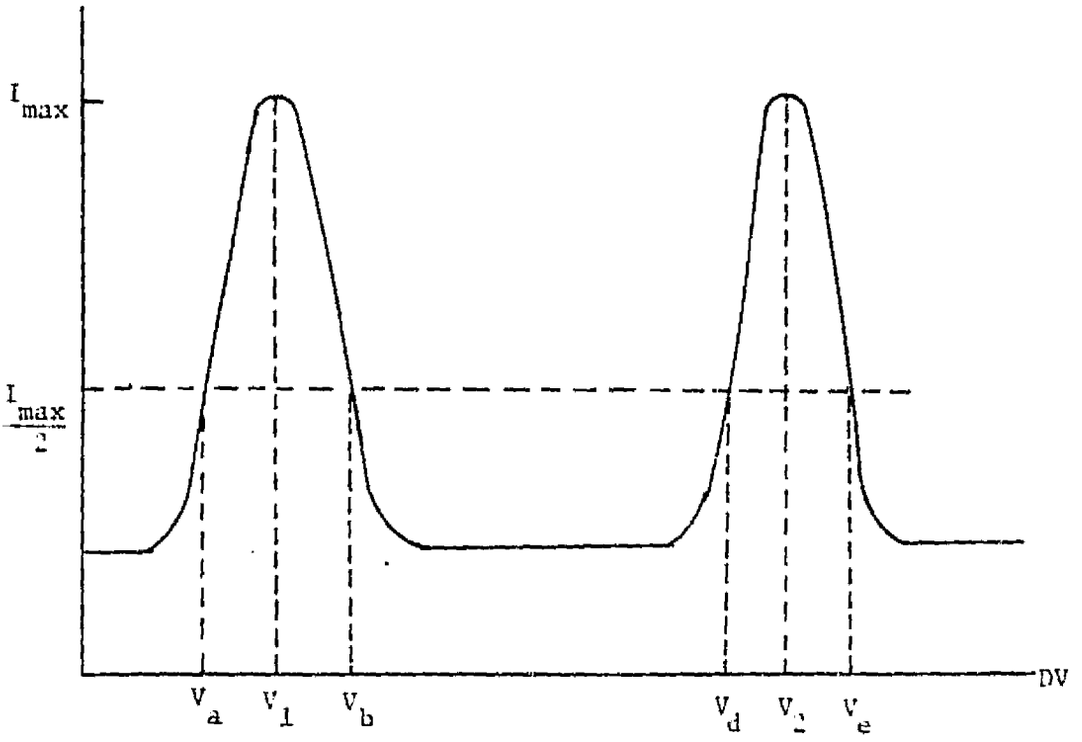

Figure 13. Plot of primary current striking the detector as a function of deflection voltage.

The difference between V_a and V_b, or V_d and V_e, is defined as the effective width of the probe beam, where the current levels at V_a, V_b, V_d, and V_e are all one half of the maximum currents measured at V_1 and V_2. Therefore it is possible to estimate the probe beam thickness by taking the ratio of $V_a - V_b$ and V_{dv} and multiplying this ratio by the distance between the two detector positions (0.8 mm). The ratio was found to be a constant, one fifth, with respect to the probe beam acceleration voltages while the magnitude of I_{max}, V_a, and V_b varied as a function of the acceleration voltage. Thus the approximate probe beam thickness was equal to about 0.15 mm. Since the detector wires were 0.12 mm thick, there was no reason to reduce the beam thickness further because the detector wire would be unable to sense any greater resolution due to its dimensions.

The same procedure, and currents versus voltage plot, was conducted for probe beams exiting the cylinder. These experiments and calculations revealed that the probe beam thickness at the exit point was about 0.2 mm and therefore the probing beam suffered little divergence in its path through the cylinder. For an accelerating potential of 10kV, V_{dv} was found to be 450 volts and $V_a - V_b$ was found to be 90 volts for the frontside case, while on the backside V_{dv} was approximately 80 volts and $V_a - V_b$ was about 20 volts. These types of measurements were easily made.

Pulse Circuitry

This feature of the system was not used for potential mapping but for deflecting the beam to arbitrary points on the dielectric

surface. Other researchers (11, 17, 27, 28) have used this pulsed beam approach for probing charged and uncharged dielectrics. Willis and Skinner (17) had a beam current on 10^{-9}A for a pulse duration of 10^{-6}s with a beam area of 5 mm^2. Johnson and McKay (27) worked with 10^{-6}A for pulse durations of 10^{-5}s, while Dobretsov (11) used single pulses of density 10^{-9}-10^{-7}A/cm^2 for 10^{-6}-10^{-5}s with a beam area of 1 cm^2. Finally, Whetten and Laponsky (28) used a primary current of 10^{-9}A for several microseconds with a current density of 1 mA/cm^2. Two authors (11, 27) were using test charges on the order of 1 pC while the other two (17, 28) could measure charges of magnitude 10^{-3} pC. The work done by this lab was with a beam area of 1.5 x $10^{-3}cm^2$, a current strength of 10^{-11}-10^{-9}A, and pulse widths of 10^{-3}-10^{-2}s. In general, we were dealing with charges on the order of 1 pC.

Figure 14 shows the schematic for the pulse circuitry used. The two TTL-7400 nand gates are connected in a set-reset flip-flop configuration where closing switch one will deliver a single chatter free pulse as shown in Figure 15. Switch two (reset) must be pushed in order to allow another pulse to be created. Basically, the flip-flop is a reliable debounce circuit. The RC high pass filter and first TTL-7404 inverter (I_1) differentiates the voltage shift from Figure 15 and generates a monostable pulse as shown in Figure 16. The pulse width is controlled by the filter time constant and is from 10^{-2} to 10^{-3}s.

The second TTL-7404 inverter (I_2) inverts the waveform of Figure 16 and drives the base of a high voltage transistor (BV_{CEO}= 1500V) with a base current strong enough to saturate the transistor. The base current is sufficient to saturate the transistor at any voltage (V_H - V_L) of interest.

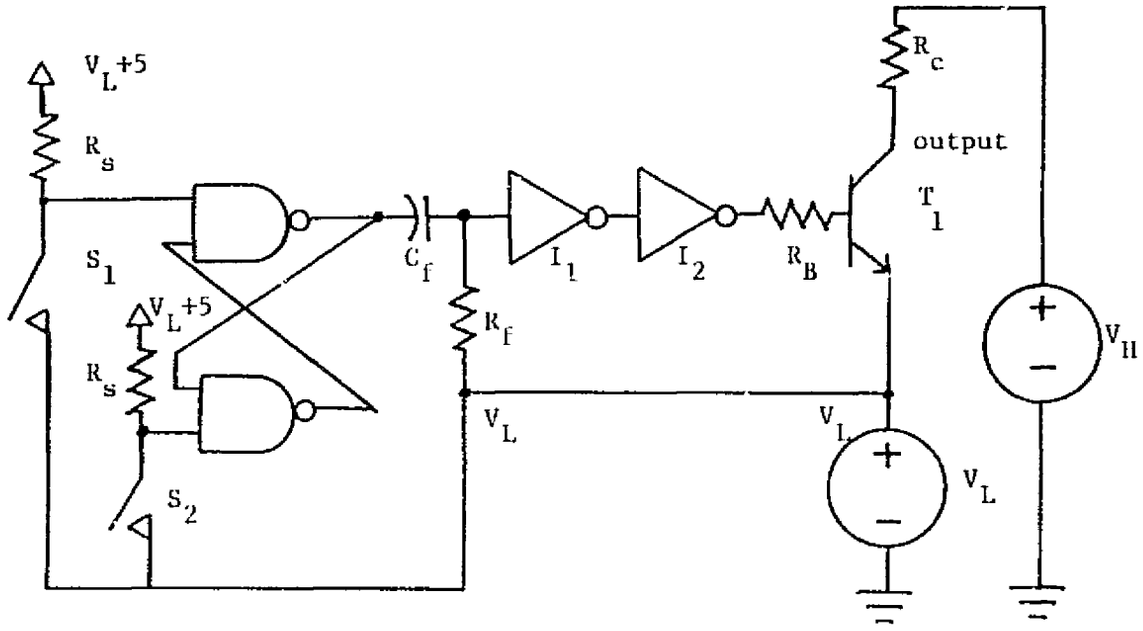

Figure 14. Pulse circuitry.

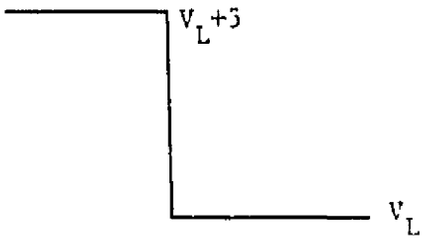

Figure 15. Output of flip-flop when S_1 is closed.

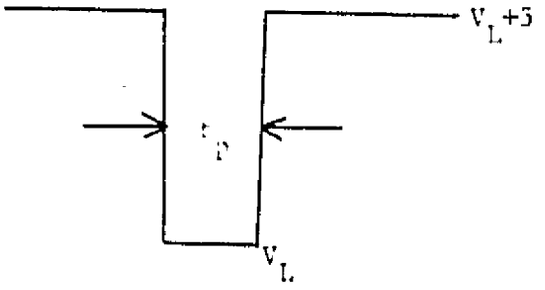

Figure 16. The output of inverter one.

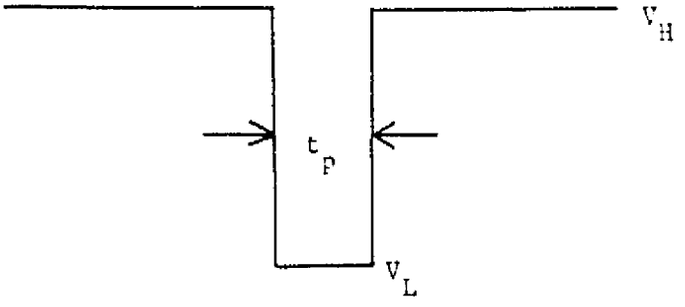

Figure 17. The final output of the pulse circuitry applied to the deflection plates.

Figure 17 shows the final waveform applied to the deflection plates when switch one, shown in Figure 14, is closed. One of the deflection plates is grounded while the other plate is connected to the collector of the transistor shown in Figure 14. Note V_L may be above, below, or at ground potential as long as $V_H - V_L \leq BV_{CEO}$.

Signal Monitoring Equipment and System Noise

The charges deposited and released from the specimens were monitored using two 600B Keithley electrometers. This data was recorded permanently using a Sanborn 320 strip chart recorder.

In the first set of experiments the probing beam impacted the detector wires for specific deflection voltages. The magnitude of the probing beam current was measured as a function of deflection voltages and these measurements were recorded for future reference. When the probing beam was reflected back to the cylinder exterior, the angle β (shown in Figure 11) could be controlled with the deflection voltage, so that the experimentalist could adjust the voltage to obtain the monitored detector current. Background current was present in these experiments as indicated in Figure 13, but maximums were easily detected if the detectors were shielded from stray currents.

The second set of experiments, which involved striking the specimen with the primary beam, did not require use of the detection wires and therefore only the specimen charge was monitored. The changes in surface charge were recorded permanently for future analysis using the strip chart recorder.

Noise present in the monitored specimen charge was partially filtered out using a simple RC low pass filter. The signal was much noisier for a charged specimen than for a discharged specimen which indicated that the origin of the noise was not necessarily external in nature, but might be associated with transient discharges between buried layers of electrons and the surface. It was noted that in one experiment, after the surface of the dielectric was bombarded once, the signal became very noisy. The exact nature of noise in the experiment was never isolated and eluded a comprehensive analysis. The noise present set a lower limit on the amount of charge that could be detected. It was possible, in a charged state, to accurately measure ($\pm$ 10%) at least 0.5 pC with greater accuracy for larger charges.

Figure 18 shows the change in the surface charge for a beam which has impacted the dielectric surface with a 10 ms pulse of magnitude 1.0 pC. The noise is represented by the small fluctuations where the step function is the important data representing charge released or accumulated by the dielectric surface. The slope is a measure of how quickly the sample was spontaneously discharging. This natural discharging was at a rate of 1 pC every few seconds, and represented a loss of 0.1% of the total accumulated surface charge during a 10 minute experiment cycle. In other words, this drifting of the surface charge caused no significant leakage of charge (and hence perturbation of assumed potentials) during the course of an experiment. There were three components present in the monitored signal: the noise, the drifting, and the step function signal. For a charged specimen the noise and drifting were present and placed constraints on the resolution obtained in

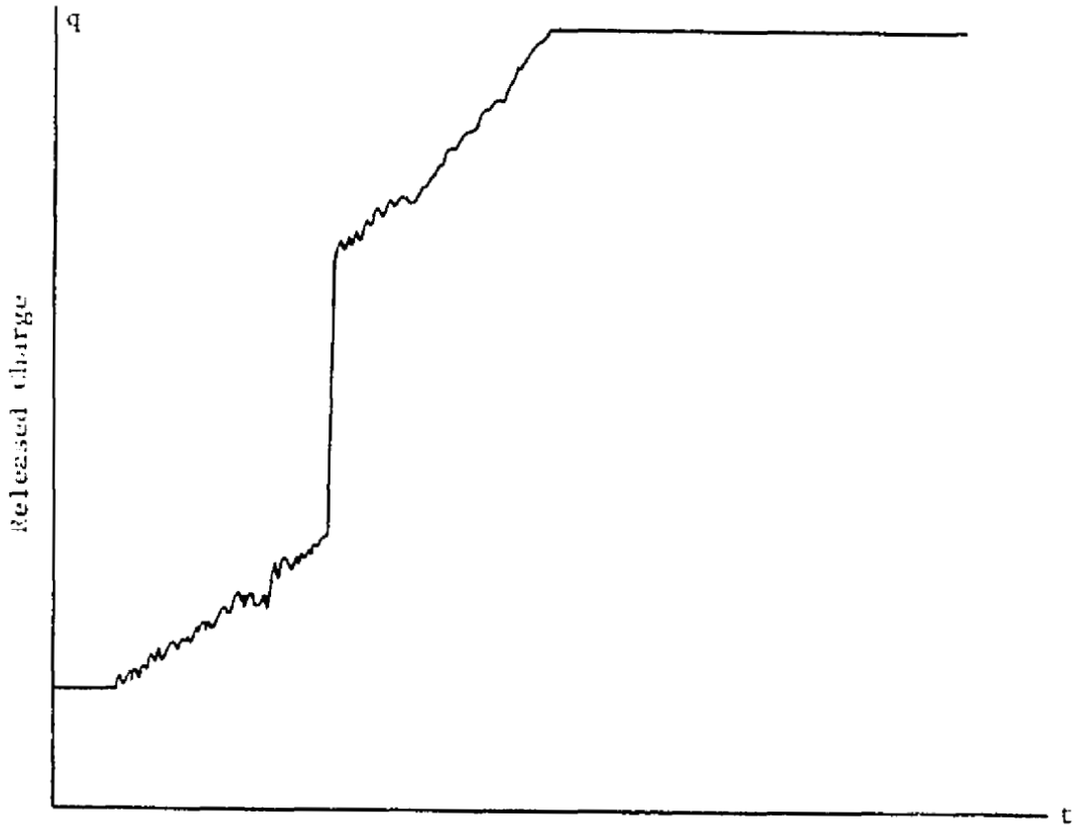

Figure 18. Plot of a typical measured charge (Q_n, Q_r) as recorded by the strip chart recorder.

measurements while for an uncharged sample the noise and drifting caused no problems.

CHAPTER III

ESTIMATION OF POTENTIAL DISTRIBUTIONS

Chapter III describes the mathematical and experimental basis used to model and measure potential distributions present on the dielectric surface due to surface charge. The first section deals with the mathematical modeling and assumptions made in approximating the surface potential. Conformal mapping (7), and DeVogelaire's method (29) of solving second order differential equations are used, along with numerical integration, to plot electron trajectories based on assumed potentials. Real measured trajectories are compared to simulated trajectories, based on assumed potentials, and a best fit of measured and simulated trajectories indicates which assumed potential is a best choice.

The second section describes how the experiments were actually conducted while Appendices B-F describe the exact step-by-step sequences used in recording data. The second section presents the procedure in a conversational manner while the data was actually taken using a strict step by step procedure listed in the Appendices. The first subsection of section two describes how surface potential maximums (at X = 0) were measured while the next subsection describes how trajectories were measured and under what constraints the measurements were made.

Methods Using Conformal Mapping and Numerical Integration

All calculations are done using a two-dimensional geometry even though the system was three-dimensional. Three-dimensional modeling

was attempted and abandoned due to computer time cost. Error in two-dimensional calculations has been estimated (30) to be negligible if the cylinder length is 2.5 times the diameter, and if the specimen length is equal to the cylinder diameter. Thus the semicircle discussed herein is a two-dimensional representation of a three-dimensional problem.

Robinson (8) describes how he used Quoc-Nguyen's (7) methods for calculating the potential and fields in the half-cylinder electrostatic region of interest. The potential and fields were calculated by a combination of a conformal mapping and an integration of a two-dimensional Green's integral (7, 30). When the one-dimensional potential function is multiplied by the normal derivative of the Green's function evaluated on a plane, the resulting function may be integrated to yield the potential at some point above the plane. Field components are found by taking the gradient of that integral. Prior to the formulation of the integral, the half-cylinder must be mapped via conformal mapping into a semi-infinite plane.

Conformal Mapping

Conformal mapping, illustrated in Figure 19, acts upon a semicircle (or half cylinder) with radius r_o and with a specimen width of $2B_o$. If the region within the semicircle is described as the W-plane (or $U + jV$), then the mapping

$$Z = \frac{2W}{1 + (W/r_o)^2} \tag{41}$$

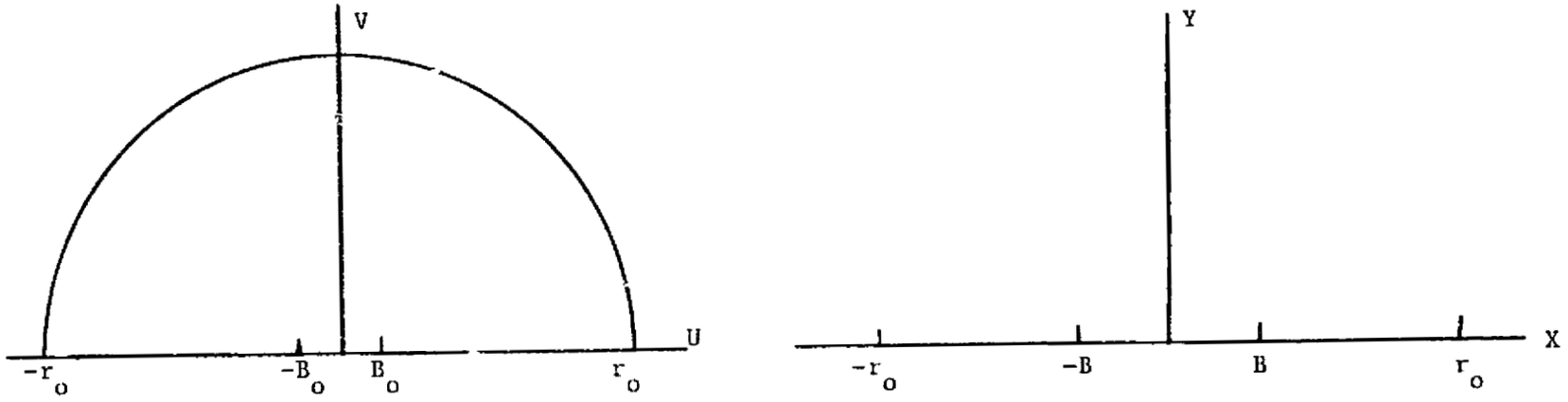

Figure 19. Conformal mapping of the original plane (U, V) into the transformed plane (X, Y).

cuts the circle at $W = ir_o$ and opens it into the upper-half plane described by Z (or X + iY). The three points $W = r_o$, 0, $-r_o$ do not move but the edges of the specimen at $W = \pm B_o$ move to new positions at $Z = \pm B$.

When B_o is small compared with r_o, then B is approximately given by $2B_o$ and the transformed specimen is then twice as wide as the original.

The potential of a point in the transformed plane is the same as the potential of the corresponding point in the original plane, but the field components calculated in the transformed plane must be transformed back to the original plane. The derivative of the conformal mapping transformation,

$$S + iT = \frac{dZ}{dW} = \frac{2\left[1 - (W/r_o)^2\right]}{\left[1 - (W/r_o)^2\right]^2} \tag{42}$$

is used to transform the field components back into the original spatial plane (U + iV).

The spatial electric field components are given by

$$E_u = SE_x + TE_y \tag{43}$$

$$E_v = -TE_x + SE_y \tag{44}$$

Surface Potential

In the transformed Z plane the potential at some point (X,Y), is equal to an integral over the specimen's surface where the potential on the surface is defined as P' (X), (assumed for each computer run).

The transformed potential then is given by Equation (45) where ϕ is just a dummy variable.

$$P(X,Y) = \frac{Y}{\pi}\int_{-B}^{B} \frac{P'(\phi)\, d\phi}{(X - \phi)^2 + Y^2} \tag{45}$$

The surface potential P'(X) is expressed for the half-cylindrical case as a polynomial in X, the transformed variable, instead of in terms of U, the real spatial coordinate. The surface potential is

$$P'(X) = \sum_{i=0}^{m} A_i\, (X/B)^i \tag{46}$$

where m is finite. From known boundary conditions it is assumed that $P'(-B) = P'(B) = 0$ and that, therefore, the sum of the even A_is is zero and the sum of the odd A_is is zero. If the surface is charged in a symmetric manner, then the surface potential is an even function in X and all odd A_is must be zero. If A_o is less than zero and d^2P'/dX^2 is positive, then it is assumed that all other even A_is are positive.

The expression describing the surface potential may be substituted into the Green's integral so that the potential at some point in the transformed Z plane becomes

$$P(X,Y) = \frac{Y}{\pi}\sum_{i=0}^{m}(A_i I_{1i}/B^i) \tag{47}$$

where

$$I_{1i} = \int_{-B-X}^{B-X} \frac{(\phi + X)^i d\phi}{(\phi^2 + Y^2)} \tag{48}$$

The electric field components are determined by taking the negative gradient of Equation (47) so that

$$E_x = -\frac{2Y}{\pi} \sum_{i=0}^{m} (A_i I_{2i}/B^i) \tag{49}$$

$$E_y = -\frac{P}{Y} + \frac{2Y^2}{\pi} \sum_{i=0}^{m} (A_i I_{3i}/B^i) \tag{50}$$

where

$$I_{2i} = \int_{-B-X}^{B-X} \frac{\phi(\phi + X)^i \, d\phi}{(\phi^2 + Y^2)^2} \tag{51}$$

$$I_{3i} = \int_{-B-X}^{B-X} \frac{(\phi + X)^i \, d\phi}{(\phi^2 + Y^2)^2} \tag{52}$$

and ϕ again is just a dummy variable for integration.

The quantities r_o, B, the assumed A_is, and a point (X,Y) (with a corresponding spatial coordinate point U,V) are specified so that the following procedure may be implemented to obtain the potential and field components within the electrostatic environment. It is necessary to evaluate the integrals in Equations (48), (51), and (52) for some assumed coefficient index i. The results are then transformed back to the original semicircle (U + iV) by using Equations (43) and (44) and noting that the potential does not change during the coordinate transformation.

DeVogelaire's Method

It is necessary to simulate electron trajectories within the half-cylindrical region if an experimentalist is to know where and with what attack an electron impacts the dielectric surface (experiments described in Chapter IV). The trajectory simulation routines are also necessary for interpreting measured reflected trajectories. The procedures just described yield electric fields which provide the accelerations required by the trajectory tracing routines described in this section.

The trajectory tracing routine used was developed by Tilley (6) and Robinson (8) based on the method of DeVogelaire (29) where the electric fields derived from conformal mapping provided the necessary electron accelerations. DeVogelaire's method applies to second order differential equations without explicit first derivatives and is correct to fourth order. The spatial and velocity components must be known at a time t_i and also the spatial coordinates must be known at the time corresponding to a half-step before t_i. Electric field components are evaluated at these points (X_i, Y_i) and a new half-step is given by

$$X_h = X_i + V_x T/2 + qT^2((3 + F)E_x - FE_{-hx})/24 \qquad (53)$$

where X is the transformed coordinate, T is the time step, V is the velocity, E is the electric field at X_i, E_h is the electric field at the prior half-step point, and q is the charge/mass ratio. The quantity F is unity (dimensionless) for most particle steps except when the size of the time step is changed. After the half-step, the fields at the new point are computed and the whole step is completed so that

$$X_{i+1} = X_i + V_x T + qT^2(E_x + 2E_{hx})/6 \quad . \tag{54}$$

Equations similar to (53) and (54) apply to the Y coordinates and are evaluated simultaneously. After a step is completed, the new velocities are evaluated from

$$V_{(i+1)x} = V_x + qT\ (E_x + 4E_{xh} + E_{(i+1)x})/6 \tag{55}$$

where a similar equation applies to the Y component of velocity.

The conformal mapping, the Green's integral, and DeVogelaire's method are all implemented using computer routines and subroutines which are described by Robinson (8). These routines were also used to set up the experiments described in Chapter IV.

Experimental Procedures Used Involving Reflected Trajectories

This section describes the experimental procedures for measuring the peak surface potential A_o and electron beam deflection γ. The first subsection describes measurements of A_o for charged samples and the second subsection shows how electron trajectories were measured and analyzed.

Determination of Surface Potential

The peak surface potential, defined earlier to be A_o, must first be determined experimentally before computer simulations can be attempted. When the surface has been charged with a flood gun acceleration voltage of, for example, V_g, the surface charge stabilizes at an

equilibrium state where, for every electron which impacts the surface one is given off. The flood gun voltage V_f corresponds to the higher of the two unity emission points in the curve, showing σ versus primary energy. The other point at which $\sigma = 1$ for polymers is usually 20 to 50 volts above the surface potential A_o and represents an unstable equili.rium.

The peak surface potential is experimentally defined to be the lowest possible primary acceleration voltage A_o which causes the slightest perturbation of surface charge. This potential A_o may be determined experimentally by the following procedure. First, the specimen is charged with a known high voltage bias on the flood gun assembly V_f. Next the middle (X=0) of the specimen is probed with a series of normally incident beams which have discrete energy steps of 10eV. The energy is increased until the monitored charge indicates the specimen has been struck.

What is referred to in literature as the critical voltage V_c (or critical energy $E_c = eV_c$) is the difference between V_f and A_o. For a charged specimen the critical energy is defined herein to be

$$E_c = e(V_f - A_o) \ . \tag{56}$$

For voltages less than the peak surface potential it was possible to cause discharging of the specimen near its edges, where the surface potentials were lower than that in the middle. Care was taken not to confuse discharging near the edges with discharging caused by striking the middle of the specimen. It was sufficient to strike the specimen with a variety of deflection voltages to insure that the center potential

had been measured and not some other potential based on impacting the surface off center. Table 1 shows the various peak surface potentials A_o (energies) for different flood beam charging potentials.

The first column in Table 1 displays each flood gun potential used while column two represents the measured surface potential for each of these charging potentials, and column three shows the energy spread ($eV_f - eA_o$) which corresponds to the critical energy in the secondary emission curve. Column four shows the normal electric field at X=0 for each case. There is an experimental error of $\pm$ 20 V associated with the measurements made in columns one and two where column three would therefore have an error spread of about $\pm$ 40 V. These results are consistent with those found by Quoc-Nguyen (10), for the estimated electric field strengths in these cases.

Reflected Electron Trajectories

Electron trajectories were determined experimentally based on four known experimental quantities: the angle α of cylindrical incidence (Figure 11), the primary beam angle β of inclination, the primary beam initial kinetic energy E_p (on entering the cylinder), and the exit angle γ for the reflected primary beam. The primary beam energy E_p and the angle α were easily determined while the angle γ was found by looking for the reflected primary beam with the detector wires. Angle β was controlled by the deflection plate voltage.

For all potential mapping the angle of cylindrical incidence was kept constant at 90° so that the primary beam could interact strongly

Table 1. Values for the flood beam potential, peak surface potential, critical voltage and surface electric field.

eV_f	eA_o	$eV_c = e(V_f - A_o)$	E_v (V/mm)
6000	4200	1800	980
8000	6150	1850	1500
10,000	8080	1920	2090
12,000	10,040	1960	2730
14,000	12,000	2000	4080

with the potential field. The initial primary kinetic energy E_p was kept at about 3keV below the flood beam energy E_f and was about 80% of the surface potential energy eA_o. The thin collimated electron probe beam was injected into the half-cylindrical electrostatic environment with an initial kinetic energy which was too low to impact the surface. Therefore the electron beam was reflected back towards the detector wires mounted on the circumference of the cylinder. The wires were set at predetermined exit angles (where γ = 144°, 126°, 108°, 90°, 72°, 54°, and 36°) and the deflection plate voltage was varied until the reflected primary beam struck a detector wire. Table 2 shows the deflection voltages corresponding to each exit position for a flood beam potential of 8kV and a probe beam voltage of 5kV. The peak surface potential at X=0 was measured to be 6150 volts for this case.

The first column shows the exit angle, the second column shows the actual deflection voltage required for the beam to strike a given detector wire and the third column is a repeat of column two where the deflection voltage (8.8 volts in this case) required to reflect the primary beam straight back is subtracted from all actual deflection voltages. It was not necessary to construct a probe gun which could precisely inject a primary beam straight into the cylinder with an actual deflection voltage of zero. The 8.8 volts in Table 2 represent the correction voltage required to center the beam. It should be noted that the angle of inclination β is zero when the deflection voltage is 8.8 volts because if β was not zero the beam would not reflect straight back to the point of origin. The adjusted deflection voltages tabulated in column three of Table 2 are multiplied by the deflection factor D (0.000432 radians/volt for a 5kV beam) and the angle β is obtained

Table 2. Injection angles, reflected angles, and deflection voltages used in potential mapping for the case where V_E = 8kV.

γ	DV	DV - DV (90°)	β (radians)
144°	+42.0	+33.2	+0.0144
126°	+33.6	+24.8	+0.0107
108°	+20.6	+11.8	+0.0051
90°	+ 8.8	0.0	0.0
72°	- 3.6	-12.4	-0.0053
54°	-16.2	-25.4	-0.0105
36°	-25.0	-33.8	-0.0146

in this manner. Next the three known quantities, α, β, and the primary energy, are used as input parameters to the electron tracing routines (8). Different coefficients in the polynomial expansion for the surface potential are assumed and the exit angles depending on the four quantities (α, β, primary energy, and coefficient choice) are tabulated. The final data is presented as a graph where the measured exit angle is subtracted from the exit angle calculated using computer simulations and plotted on the ordinate while the measured exit angle is plotted alone on the abscissa.

Numerical Values for Surface Potentials

Figures 20 through 24 display the processed data for a flood beam energy of 6kV, 8kV, 10kV, 12kV, and 14kV, respectively.

Equations (56) through (60) summarize how the surface potential depends on the flood beam energy and position.

$$V(X) = 4200[1 - (X/B)^8] \tag{56}$$

$$V(X) = 6150[1 - (X/B)^6] \tag{57}$$

$$V(X) = 8080[1 - .5(X/B)^4 - .5(X/B)^6] \tag{58}$$

$$V(X) = 10040[1 - (X/B)^4)] \tag{59}$$

$$V(X) = 12000[1 - .5(X/B)^2 - .5(X/B)^4] \tag{60}$$

The cases where V_f = 8kV (A_o = 6150) and V_f = 12kV (A_o = 10040), were used to determine how to choose α and β in order to impact the specimen at the desired angle θ and some point on the surface X.

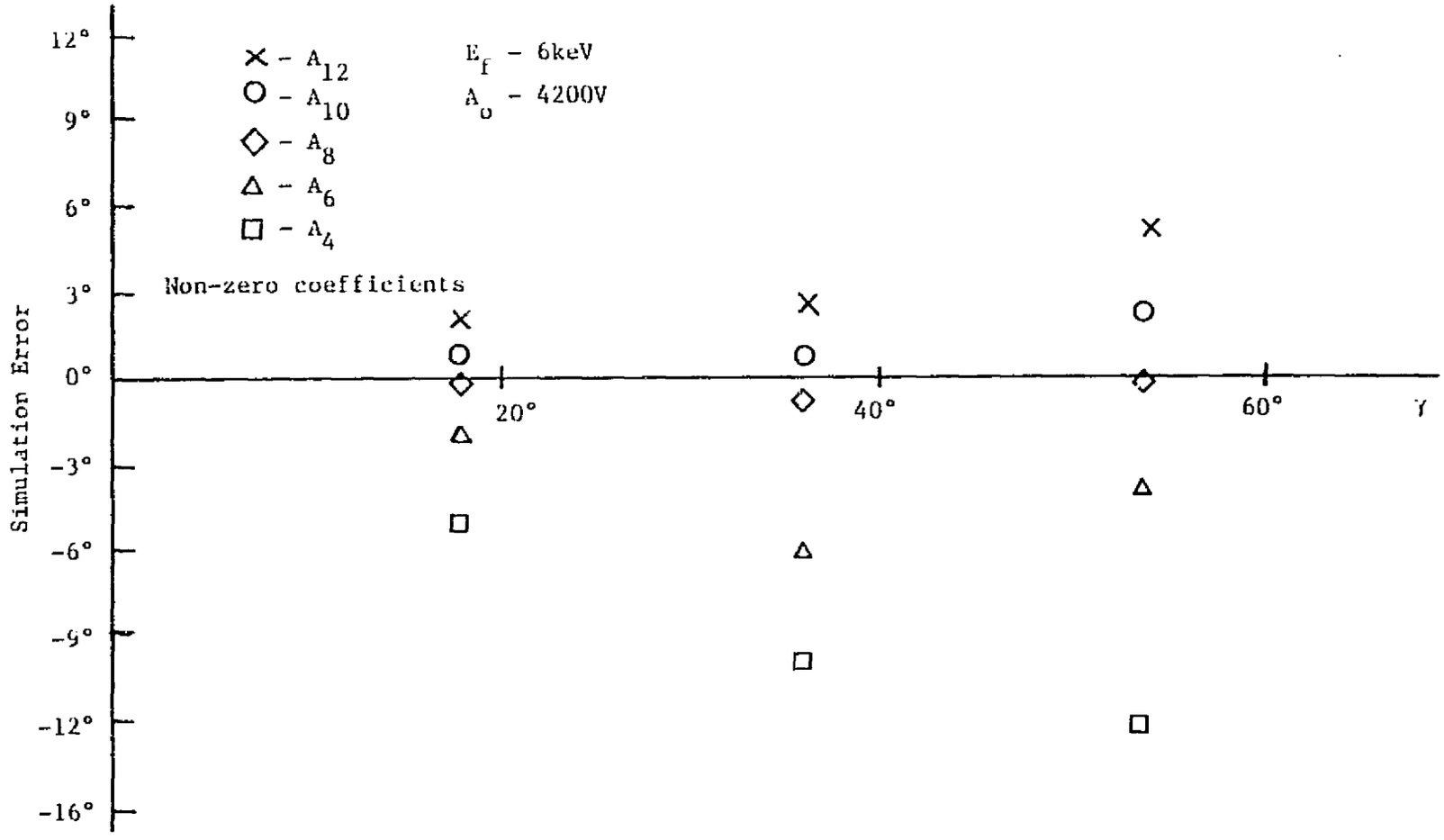

Figure 20. Comparison of simulation and experiment for reflected trajectories where E_f = 6keV. Simulation error is plotted on ordinate while abscissa shows measured exit angle γ.

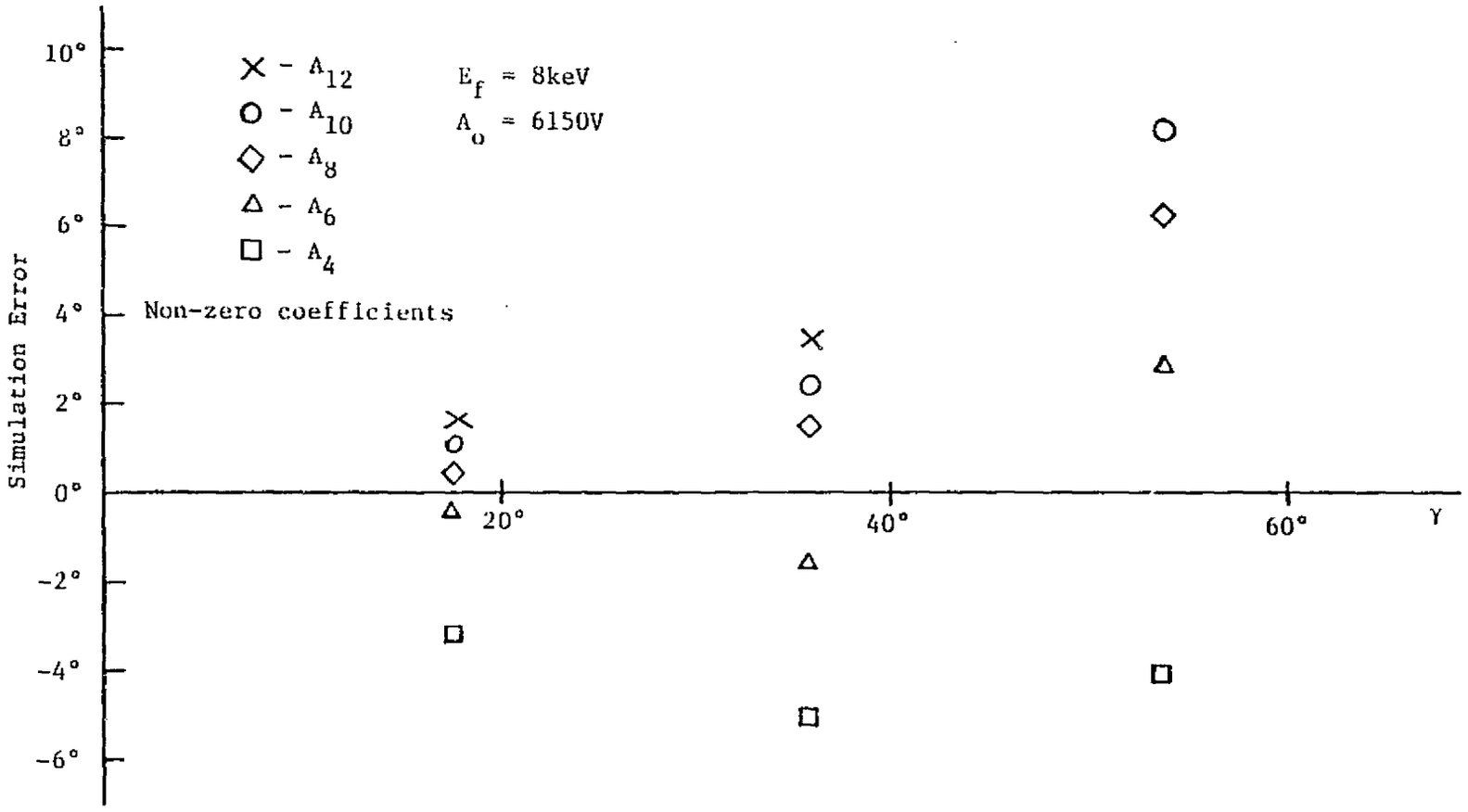

Figure 21. Comparison of simulation and experiment for reflected trajectories where E_f = 8keV. Simulation error is plotted on ordinate while abscissa shows measured exit angle γ.

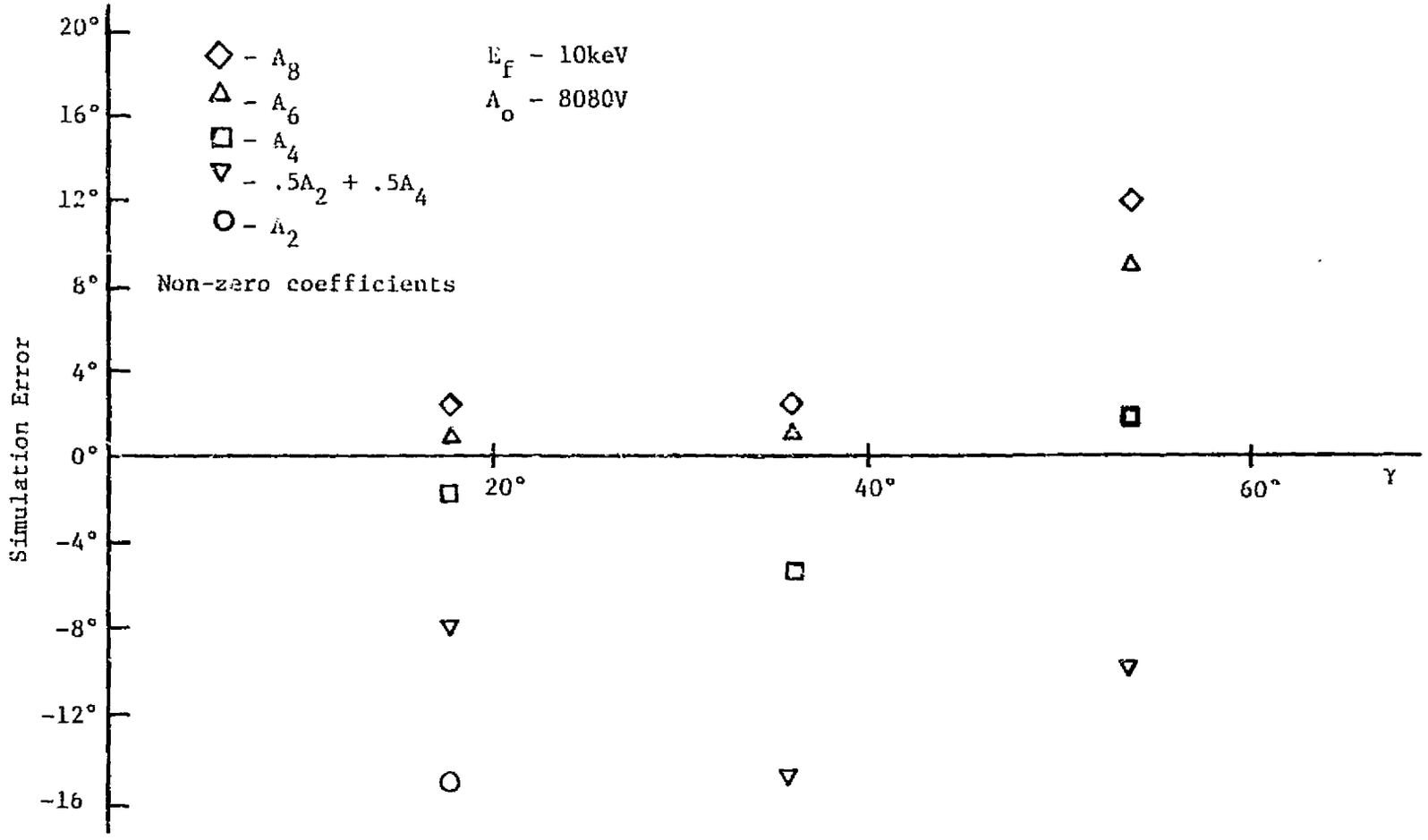

Figure 42. Comparison of simulation and experiment for reflected trajectories where E_f = 10keV. Simulation error is plotted on ordinate while abscissa shows measured exit angle γ.

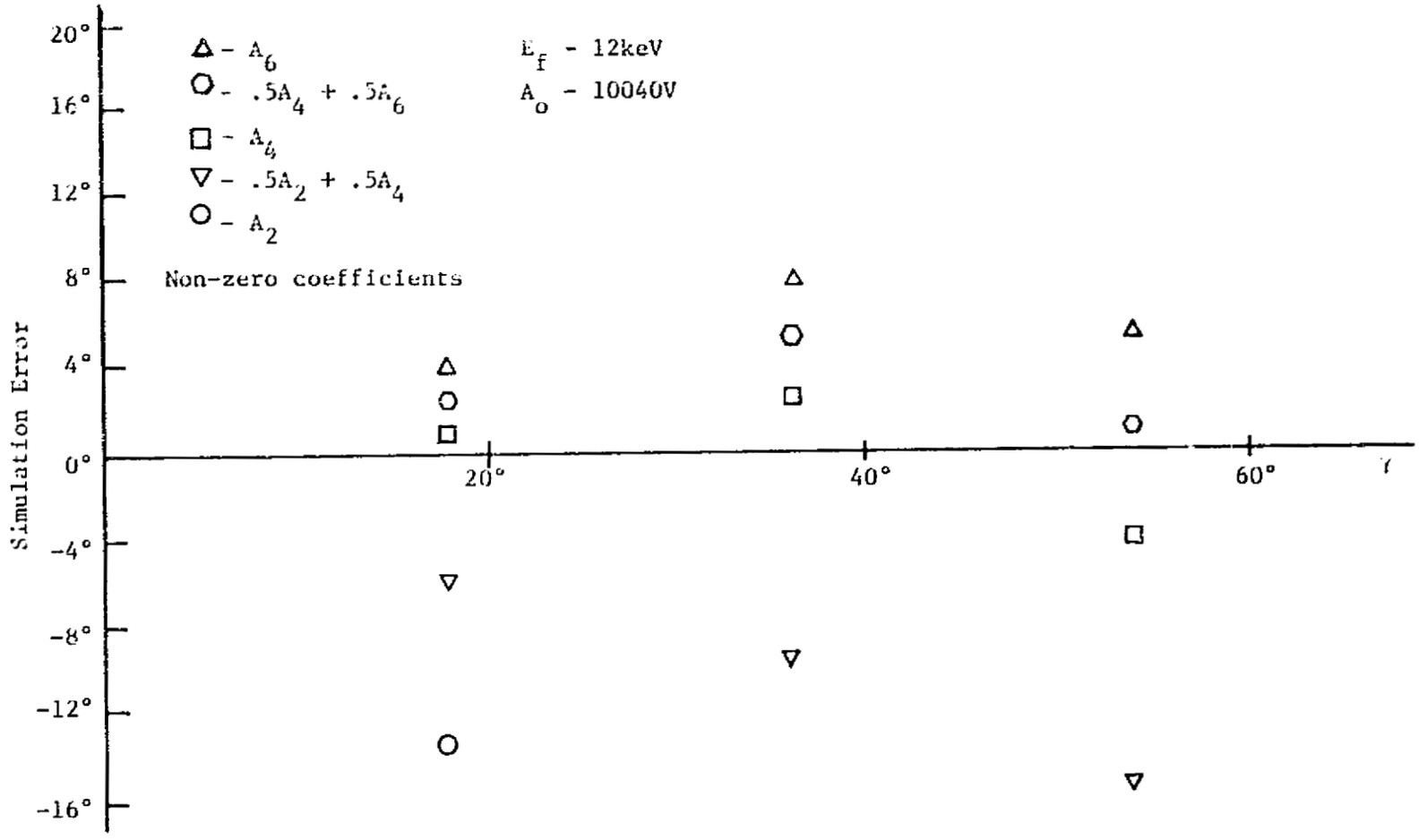

Figure 23. Comparison of simulation and experiment for reflected trajectories where E_f = 12keV. Simulation error is plotted on the ordinate while abscissa shows measured exit angle γ.

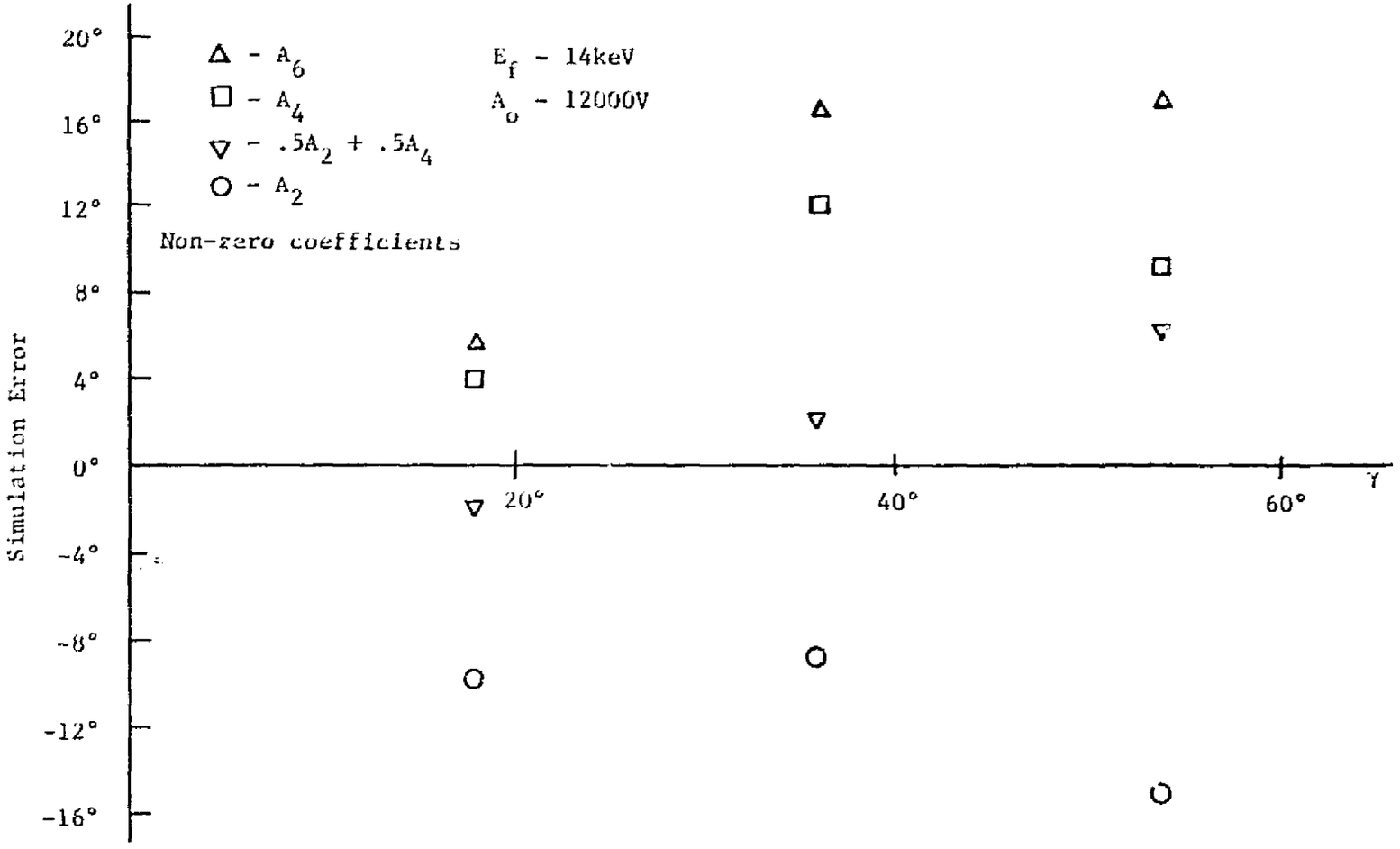

Figure 24. Comparison of simulation and experiment for reflected trajectories where E_f = 14keV. Simulation error is plotted on the ordinate while abscissa shows exit angle γ.

Chapter IV presents results which were generated using the potential functions as described by Equations (57) and (59).

CHAPTER IV

MEASUREMENTS OF SECONDARY EMISSION

Chapter IV describes how secondary electron emission experiments were conducted and what criterion was used for interpreting data and converting measurements into a plot of σ versus the primary energy. Section one explains how the magnitude of the primary beam charge packet is estimated. The first subsection explains how the critical energy E_{co} was determined for an uncharged sample. The second term explains how the exponent n, referred to in Equation (23), was determined experimentally. The last subsection indicates how the total primary beam charge was estimated from the measurements described in the first two subsections.

The second section describes procedures used in determining σ as a function of primary energy and angle (θ).

Estimation of the Primary Beam Charge

It was necessary to measure the critical energy for an uncharged specimen (E_{co}) in order to estimate the amount of charge directed towards the surface. Evaluating the exponent n was also necessary and this was based on measurements outlined below. The calculation of the primary impacting charge Q_p (or eN_p) requires the use of E_{co} and n which are the parameters of the theoretical model and the measurement of the charge induced in the substrate of the specimen.

Measurement of the Critical Energy

One experiment not attempted in the work of Quoc-Nguyen (10) was a measurement of the critical energy for an uncharged specimen, defined herein to be E_{co}. This measurement was important because the method used to estimate the primary charge directed at the sample depended on knowledge of the critical energy.

Large packets of primary charge impacted the center of the uncharged specimen with primary energies in the range of 1.3keV to 1.7keV. The accumulated (charging) or released (discharging) charges were monitored and recorded taking care not to strike the same area twice with the primary beam. After a set of measurements was made, the sample was discharged and the same procedure was repeated to insure reproducible results.

It was possible to find a primary energy range where charge was neither accumulated nor released by the specimen even though a relatively large amount of charge (200 pC) was used to bombard the surface. At 1.45keV the specimen just barely displayed discharging (0.5 pC released) while at 1.55keV the specimen just barely showed charging. Between these voltages no clear step function signal could be discerned due to drifting and noise present in the signal. Therefore the value of 1.5keV has been assumed to represent the uncharged critical energy.

Determination of the Exponent n

The technique used to determine n in Equation (23) for FEP-Teflon was to measure the amount of charge collected by a perfect

primary absorber (the collector) and compare this to the amount of charge deposited on the uncharged specimen at a fixed primary energy. The collector was made of stainless steel shim stock which had been roughed up with 320 sandpaper and coated with black soot. The collector was a rectangular box made with dimensions, 6 mm x 12 mm x 12 mm, and with an opening at the top (6 mm x 12 mm plane) where electrons entered. The collector was mounted within the cylinder 2 mm from the specimen edge and was electrically connected to the external world through well-shielded cables and connections.

It was possible to pulse the primary beam onto the collector and then onto the specimen for equal pulse widths and determine σ from the collected charges. It should be emphasized that this method ignores any charges which might leave the collector surface when it has been bombarded. At the primary energies which were used, we assumed that for the collector σ is very small and therefore negligible. The charge collected by the collector is defined to be Q_c while the charge collected by the sample is defined to be Q_m. These two experimentally measured quantities can be used to estimate σ for high energies (4keV or greater).

$$\sigma = \frac{Q_c - Q_m}{Q_c} \tag{61}$$

Equation (61) was set equal to Equation (23), and the only unknown, n, was determined. It was necessary to make this measurement for a variety of primary energies, while for each measurement the specimen had to be discharged to avoid errors which might have been caused by accumulated charges deposited during surface probing.

The value of n so determined was found to depend on the amount of time the system was under vacuum and it stabilized at a value of from 0.55 to 0.60 when the system was under vacuum for about five days. This measurement was critical and was the basis for modeling to follow. It was instructive to note that Matskevich (34) estimated n to be 0.725 for most polymers while the data of Willis and Skinner (2) estimates n to be 0.63 for P.T.F.E.-Teflon, and n = 0.5 for Polyamide (Kapton). Therefore the value of n for FEP-Teflon (0.6 - 0.55) was found to be in the same basic range as n found for other dielectric polymers investigated by other researchers.

Table 3 is a list of the charge measured by the specimen Q_m, the charge measured by the collector Q_c, with σ and n computed for each separate primary energy.

Once n was found the collector was removed from the specimen's electrostatic environment and the primary charge Q_p was found using a method depending on knowledge of E_{co}, n, E_o, and Q_m. The reason the collector was not used in all experiments was that it perturbed the environment to an intolerable degree.

Calculation of Primary Beam Charge

This subsection explains the method used to determine the amount of charge present in the primary beam charge packet. With a known value of n and the use of approximations justified in Chapter I, it was possible to estimate the magnitude of the charge present in the primary beam packet defined as Q_p. It should be noted that once the collector

Table 3. Charges measured by collector Q_c and specimen Q_m which yield σ and n as a function of probing energy.

E_p (keV)	Q_m (pC)	Q_c (pC)	σ	n
4	6.00	12.75	0.53	.61
5	6.25	12.75	0.51	.55
6	3.30	5.75	0.43	.58
8	2.25	3.75	0.40	.55
10	6.50	4.20	0.34	.57

(described in the last subsection) is removed from the system, Q_p is no longer a directly measurable quantity. However, Q_p can be estimated by the procedure outlined below. In essence, Q_p and Q_c are the same, yet the subscript c means that this charge (Q_c) was determined experimentally, while the subscript p emphasizes the fact that the quantity Q_p was no longer a directly measured (by electrometers) quantity. Q_p is derived from measured quantities, but it is not itself a single measurement as Q_c was. It is necessary to define six quantities, stated below, so that any confusion of terminology may be avoided.

Q_m--This measured charge was obtained from a step function output recorded by the strip chart recorder and was always negative. Q_m was measured when the primary beam was pulsed onto the uncharged specimen with an energy of at least 4keV.

Q_p--This charge was deduced from approximations, a knowledge of n and E_{co}. This quantity is not directly measured as is Q_m.

Q_c--This is the charge collected by the collector described in the previous subsection and is a directly measurable quantity which should be equal to Q_p.

Q_n--The amount of negative charge measured by an electrometer when the surface of a charged specimen was impacted. This symbol indicates that the previously charged specimen has been further charged locally by the probe beam.

Q_s--This is the amount of charge reflected back from the uncharged specimen when it has been struck by a primary beam of energy greater than E_{co} (1500 eV). This is a measure of the secondary electrons emitted from an uncharged specimen. Q_s is not a directly measurable quantity.

Q_r--This is the amount of positive charge measured by the electrometer when the primary beam impacts the surface of a charged dielectric. In this case σ must exceed one since discharging is occuring when the electrometer measures positive charges. It should be noted that positive charge is not really being deposited on the surface, but more electrons are leaving the surface than are striking it, which the electrometer senses as a positive charge.

By equating Equation (23) with Q_s/Q_p we have a means of expressing Q_p in terms of the measured quantities Q_m, n, E_{co}, and E_o (the primary kinetic energy of impact). Equation (62) expresses this equality.

$$\sigma = \delta = \left(\frac{E_{co}}{E_o}\right)^n = \frac{Q_s}{Q_p} \tag{62}$$

This equation states that the secondary charge divided by the primary charge is equal to the theoretical (and experimentally verified) relation $(E_{co}/E_o)^n = \delta$. Here it is necessary to stress that the elastically and inelastically reflected electrons have been included experimentally in Equation (62) though theoretically the symbol δ includes only true secondary electrons. However, the distinction between δ and σ is not important for determining Q_p.

The following equation is based on the law of charge conservation. Equation (63) states that the primary charge aimed at the specimen surface must equal the sum of the measured charge deposited on the surface (Q_m) and the amount of charge that left the surface (Q_s).

$$Q_p = Q_m + Q_s \tag{63}$$

The variables Q_m, Q_p, and Q_s are all different functions of primary beam energy. What is important to note is that Q_m is a reliable measurable quantity at discrete energies and that Q_s can be expressed in terms of Q_p at high primary energies as $(E_{co}/E_o)^n$. Rewriting Equation (63) in light of the above argument we have

$$Q_p = Q_p(E_{co}/E_o)^n + Q_m \tag{64}$$

where the only unknown is Q_p which may be solved for directly as

$$Q_p = \frac{Q_m}{[1 - (E_{co}/E_o)^n]} \tag{65}$$

and where Q_m, E_{co}, E_o, and n are all experimentally known quantities.

Therefore, by measuring the amount of charge (Q_m) deposited on the uncharged specimen surface at some specific energy E_o, it is possible to estimate the primary charge to an accuracy which depends on the uncertainty of E_{co} and n.

Perturbation of Surface Charge and Fields

Obtaining a value for σ depended on measuring the quantities Q_n and Q_r. It was desirable to make Q_n and Q_r easily detectable relative to the noise level yet not so high a level as to perturb the original surface charge density Q_o.

When the specimen surface was charged with the flood gun the total accumulated negative charge was measured for each experiment. Table 4 tabulates the flood gun energy, E_f, the total surface charge

Table 4. Values of total surface charge, surface charge density and local charge.

E_f (keV)	Q_t (C)	Q_o (C/cm^2)	Q_a (pC)
8	2.7×10^{-7}	8.4×10^{-8}	126
12	4.2×10^{-7}	1.3×10^{-7}	195

Q_t, the average surface charge density, Q_o, and the amount of surface charge present over the area of the probing beam Q_a, for the two cases studied.

Q_o is found by dividing the total surface charge by the surface area of the specimen (3.2 cm^2) and Q_a is found by multiplying Q_o by the area of the probing beam (1.5 x 10^{-3}cm).

In all experiments Q_n and Q_r were kept within 2% of Q_a so that the localized surface charge density was not perturbed greatly by the probing beam. For obliquely incident probing beams the area of impact would be spread and thus Q_a would be larger. The beam spreading provided less perturbation of surface charge yet then the surface potential sometimes varied over the area of impact. Thus the beam spreading had good and bad aspects.

The primary beam current based on typical experimental values is given by

$$I = \frac{Q_p}{t_p} = \frac{2pC}{20mS} = 10pA \qquad (66)$$

where I is the beam current, Q_p is the test charge and t_p is the pulse width of the probe beam. This current does not perturb the electrostatic fields significantly and such perturbations are ignored.

Procedures Used to Measure σ as a Function of Angle

The following subsections describe the experimental procedures implemented in gathering data used to calculate the secondary electron emission coefficient σ as a function of primary energy and angle of incidence θ. The first subsection describes how measurements were taken

for normally incident electrons ($\theta = 0°$). The second subsection explains what modifications were used to record data for obliquely incident electrons, and section three presents and discusses the results for each case.

Measurement of σ for Normal Incidence

First, it was necessary to impact the uncharged specimen with a beam of some fixed primary energy. From that the amount of primary charge was calculated for some specific energy E. Next, the specimen surface was charged up to a desired potential by following the procedures outlined in Chapter II and tabulated in the Appendices. The cylinder was rotated to a position where the window which permits charging was underneath the platform. The high voltage V_H on the pulse circuitry was selected and the probe beam was turned on.

It was necessary in these experiments to know at what voltage to set V_L so that the primary beam would impact the surface at X = 0. For normal incidence this was not difficult since the reflected trajectories referred to in Chapter II indicated what deflection voltage would force the primary beam to impact the center of the specimen. The surface of the dielectric was impacted all across its surface to insure reasonable results and also to investigate how the surface potential varied as a function of position. Therefore a measurement of charge (Q_r or Q_n) was recorded corresponding to the same primary energy used to impact the uncharged surface. If the surface accumulated a negative charge, then the equation used to calculate σ is given by

$$\sigma = 1 - Q_n/Q_p \ . \tag{67}$$

Here Q_n is the accumulated negative charge measured by the electrometer and Q_p is as previously defined.

If the surface of the dielectric releases charge on impact then the equation used to calculate σ is

$$\sigma = 1 + \frac{Q_r}{Q_p} \tag{68}$$

where Q_r is the positive released charge measured by the electrometer. Therefore measurements were made in the above mentioned procedure and a value of σ could be found for any arbitrary flood gun potential and probe beam potential up to 19kV, which was the operating limit of our experimental system.

Measurement of σ for Oblique Incidence

The same basic procedure was followed for the obliquely incident case as the normally incident case, except that the cylindrical angle of incidence, α, had to be chosen properly so that the probing beam would impact the surface at various angles of incidence θ. It was necessary to use reverse trajectory computer simulations, which would start a particle at X = 0 with the desired angle of impact (23° or 45°) and which would trace a path out of the system for a specific impact energy.

The exit angle of the reverse trajectory would then be used to experimentally inject the probing beam into the system with the right cylindrical angle of incidence, α, to obtain the desired final impact angle θ. Table 5 shows the angles of cylindrical incidence α

Table 5. Table of cylindrical angles of incidence and inclination angles for the oblique incidence experiments.

		θ = 45° at X = 0			θ = 23° at X = 0		
E_p (keV)	E_o (keV)	90° - α (degrees)	β (milliradians)	Motor Setting (degrees)	90° - α (degrees)	β	MD (degrees)
6.4	.25	18.0	6.0	18.0	9.3	3.2	9.0
6.6	.45	22.5	7.5	21.6	11.6	4.0	10.8
7.2	.95	29.5	10.0	28.8	15.0	5.1	14.4
7.6	1.45	32.5	11.0	32.4	16.4	5.4	16.2
8.0	1.85	34.3	11.5	34.2	17.3	5.6	18.0
8.2	2.05	35.0	11.5	34.2	17.6	5.6	18.0
8.5	2.35	35.9	11.5	36.0	18.1	5.6	18.0
9.0	2.85	37.1	11.5	37.8	18.6	5.6	18.0
9.5	3.85	38.1	11.0	37.8	19.1	5.4	19.8
10.0	3.85	38.8	10.8	39.6	19.5	5.2	19.8
11.0	7.85	39.9	10.3	39.6	20.0	4.9	19.8
12.0	5.85	40.7	9.8	41.4	20.3	4.5	19.8
13.0	6.85	41.3	9.3	41.4	20.6	4.4	19.8
14.0	7.85	41.7	8.7	41.4	20.8	4.0	21.6
15.0	8.85	42.1	8.2	41.4	21.1	3.8	21.6
16.0	9.85	42.5	7.8	43.2	21.4	3.7	21.6

computed for the various specified impact energies as required by a surface potential measured to be $V(X) = 6150[1 - (X/B)^6]$ volts. This is the case for an 8keV flood beam energy where the peak potential at X = 0 is 6150 volts. Column one represents the probing beam energies used and column two indicates the difference between probing beam potential and peak surface potential. Columns three, four, and five are for the case where the probing beam impacts the specimen at X = 0 with an incidence of 45°.

Column three tabulates the off-center angle at which the probing beam will enter the cylinder. The angles tabulated in column three are not α, the cylindrical angle of incidence, but 90° - α. This was done so that the reader can see how 90° - α approaches θ as the primary energy is increased. Column four tabulates β, the angle of inclination (in milliradians), which must be used in order to strike the specimen at X = 0. Column five displays the discrete motor drive positions which were used to inject the probing beam since the exact values in column three could not be realized due to the fact that the platform could only be moved in increments of 1.8° per step. Columns six, seven, and eight are a repeat of columns three, four, and five except that they are for the case where θ = 23° at X = 0. A similar set of angles were used to conduct experiments where the surface potential was equal to $10040(1 - (X/B)^4)V$ but these figures are excluded from this report.

In order to conduct an oblique incidence experiment it was first necessary to aim the probing beam at the platform with the correct cylindrical angle of incidence α, and then pulse the probing

beam onto the specimen. A wide range of deflection voltages (V_L) were used in order to impact the surface of the specimen from X = 0 to the edge of the specimen. The released charges, Q_r, would increase gradually with distance to a maximum and then fall off sharply as the edge of the specimen was approached.

The abscissa on Figure 25 shows the X coordinate, the deflection voltage, and the angle of incidence associated with a 9.5kV probe beam and a surface potential where $V(X) = 6150(1 - (X/B)^6)$. The angle of incidence, θ, and the values of X are obtained from computer simulations as described by Robinson (8). The simulations use the two entry angles α and β (dependent on deflection voltage), and generate X and θ as a function of α and β. Next the value of σ obtained for normal incidence at the primary energy of 9.5keV ($\sigma = 0.70$) is divided by $\cos(\theta)$ and this is shown as a solid curve in Figure 25. The ordinate shows the value of σ, as a function of theory (solid line), and experimental data (circles), while also showing the normalized surface potential.

In the construction of Figure 25 it was necessary to adjust all of the data points by 0.2 mm to the left. This was necessary since there was a slight mechanical misalignment of the probe gun relative to the cylinder. Figure 25 was constructed by laterally shifting all of the original data points by the same amount.

Table 6 lists values of X, θ, V(X), sec(θ), the theoretical value of σ and the experimental value of σ for the case shown in Figure 25.

The drop in the surface potential in the region 2 mm $\leq$ X $\leq$ 3 mm is the reason why the theoretical curve shown in Figure 25

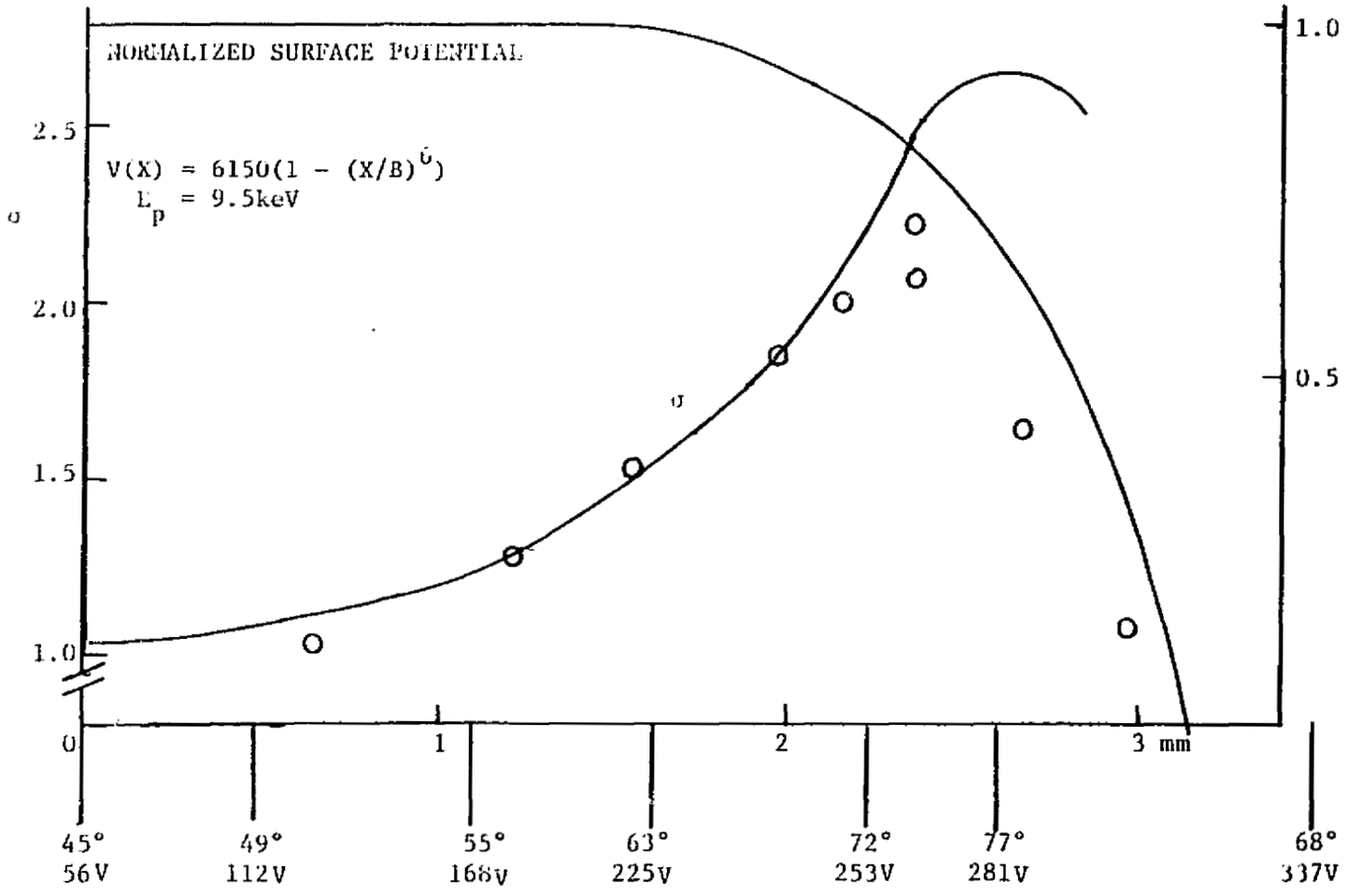

Figure 25. Comparison of experimental data with theory for E_p = 9.5keV and $\theta(X=0) = 45°$. Trajectory parameters are indicated on the abscissa.

Table 6. List of impact parameters for Figure 25 where beam energy is 9.5keV and peak surface potential is 6.15kV.

X	θ (degrees)	V(X)	$\frac{1}{\cos\theta}$	σ theory	σ experiment
- .46	49.0	6150	1.53	1.10	1.00
-1.10	55.3	6150	1.76	1.27	1.23
-1.34	59.4	6150	1.96	1.41	1.35
-1.60	63.1	6150	2.20	1.58	1.52
-2.23	72.6	5400	3.34	2.00	2.10
-2.55	77.3	4300	4.45	2.40	1.50

flattens out. The impact energy E_o in this region is equal to $E_p - eA_o(1 - (X/B)^6)$ and increases with X. The secondary emission coefficient may be approximated by Equation (23) where $\sigma = (E_c/E_o)^n$ or by extrapolating between the data points for normal incidence. The theoretical curve is obtained by finding σ at various values of X (2 mm to 3 mm) and dividing this value by cos(θ) for each X. In the region where 2.4 mm $\leq$ X $\leq$ 2.9 mm, changes in the two factors offset one another.

The agreement between experimental data and theory is good up to 2 mm but beyond this the data and theory diverge. One reason why the data and theory might diverge at X = 2.2 mm is that the probing beam is impacting at about 72° and the effective impact width is 0.5 mm. At 77° the effective width is 0.7 mm which implies that the assumptions used to create the theoretical curve are in question. The computer trajectory tracing routines are for primary beams which are of infinitesimal width and this does not effectively model the real electron beam at high angles of incidence.

Another possible explanation for the divergence is that in the region 2.2 mm $\leq$ X $\leq$ 3.0 mm the tangential fields are at least as strong as the normal fields. In general the magnitude of the fields near the edge are greater than near the center of the specimen.

Figure 26 shows a similar set of data points with a probing beam energy of 7.2keV and an angular attack of 45° at X = 0. It was necessary to adjust the data points to the left by 0.1 mm. Table 7 shows X, θ, V(X), sec(θ), the theoretical value of σ and the experimental value of σ for the parameters indicated by Figure 26.

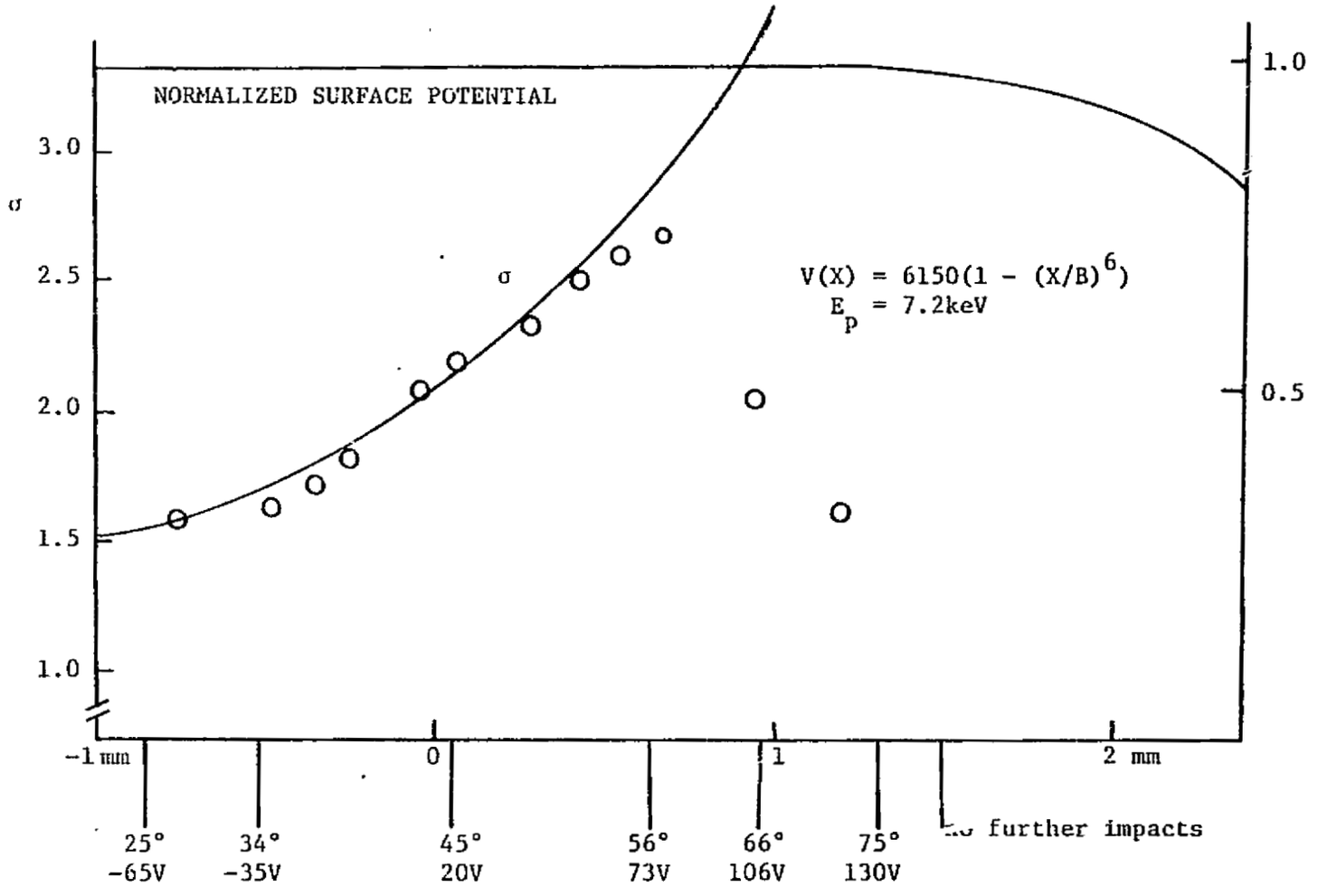

Figure 26. Comparison of experimental data with theory for E_p = 7.2keV and $\theta(X=0) = 45°$. Trajectory parameters are indicated on the abscissa.

Table 7. Table of impact parameters for Figure 26 where beam energy is 7.2keV and surface potential is 6.15kV.

X (mm)	θ (degrees)	V(X) (volts)	$\frac{1}{\cos\theta}$	σ theory	σ experiment
-0.90	24	6150	1.09	1.58	1.6
-0.53	34	6150	1.21	1.81	1.75
0.00	45	6150	1.41	2.12	2.20
+0.63	56	6150	1.79	2.68	2.6
+1.00	66	6150	2.46	3.69	2.0
+1.18	72	6150	3.24	4.85	1.8
+1.28	75	6150	3.86	5.80	1.3
+1.42	80	6100	5.76	8.64	1.0

The agreement between theory and experiment is good up to angles of incidence approaching 56°. For larger angles the agreement is poor. Tangential electric fields in the region of impact are at most 20% of the normal fields, therefore it is unlikely that the tangential fields are the cause of the disagreement. It is likely that the spreading of the beam is the reason the agreement is poor for $\theta > 56°$. Computer simulations indicate that the probing beam will be unable to impact the surface for $X > 1.45$ mm for the α and β used. As the probing beam approaches the specimen in the range $0.7 \text{ mm} < X < 1.45 \text{ mm}$, for large angles of incidence, part of the beam strikes the surface while part of it reflects away. This is one possible explanation for the divergence of experimental data and theoretical models.

Figure 27 shows data for a primary beam energy of 7.2keV and an impact angle of 23° at $X = 0$. The data points were shifted 0.3 mm to the left due to beam alignment problems. Table 8 lists X, θ, V(X), $\sec(\theta)$, the theoretical value of σ, and the experimental value of σ. No flattening of the theoretical curve is shown (contrary to Figure 26) because the drop in surface potential is not significant in the region where the theoretical curve is shown.

In the region where $0 \text{ mm} < X < 1.5 \text{ mm}$ the agreement between theory and experiment is adequate yet beyond this region the measured data does not agree with theoretical predictions. Once again beam spreading and tangential electric fields could be the source of divergence. It appears as if σ had saturated at the value of 2.5 and remained constant regardless of the angular dependence. In all

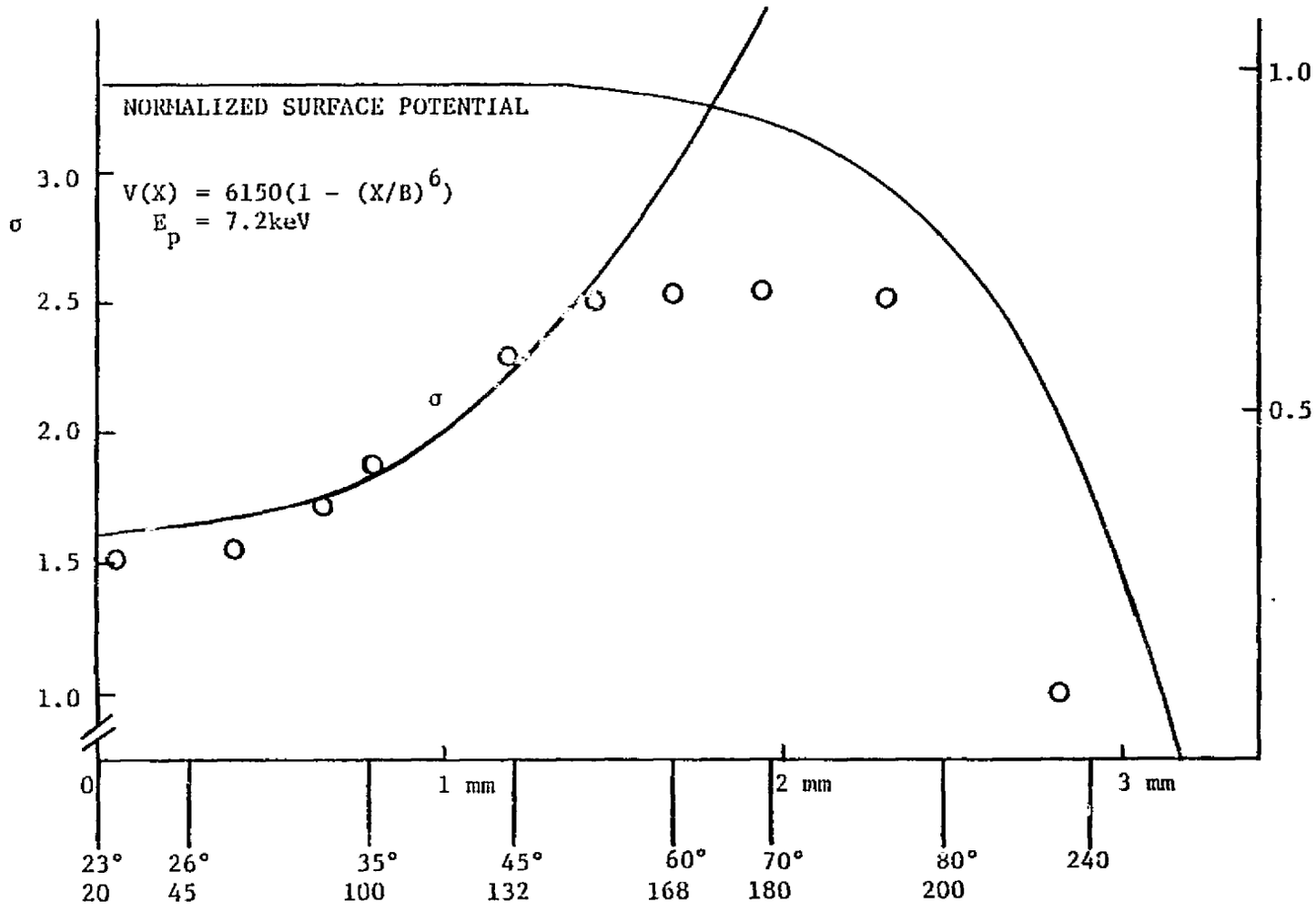

Figure 27. Comparison of experimental data with theory for E_p = 7.2keV and θ(X=0) = 23°. Trajectory parameters are indicated on abscissa.

Table 8. Table of impact parameters for Figure 27 where $\theta = 23°$ at X=0 and $E_p = 7.2$keV.

X (mm)	θ (degrees)	V(X) (volts)	$\frac{1}{\cos\theta}$	σ theory	σ experimental
0.00	23	6150	1.10	1.65	1.60
.24	26	6150	1.10	1.67	1.65
.74	34	6150	1.21	1.81	1.80
1.18	45	6150	1.41	2.12	2.20
1.66	60	6010	2.00	3.00	2.50
1.95	70	5800	2.92	4.41	2.40
2.40	80	4990	5.76	5.76	1.80

emission experiments for a surface potential where $V(X) = 6150(1 - (X/B)^6)$ the emission coefficient never exceeded 2.6 regardless of θ.

It is improbable that the term exp(-Q), as it appears in Equation (37), is the cause of the discrepancy. From range data taken from Katz, et al. (1), for polymers similar to FEP-Teflon (Kapton, PTFE-Teflon), an estimate of R is found to be 350 Å at a primary energy of 1keV (the present case). We have assumed $K_2 = 350$ Å/keV in Equation (38) and that $n = 0.58$. If $X_s = 50$ Å, at worst case, then $R/X_s = 7$ and the correction term becomes negligible for angles less than 65° for $E_o = 1$keV. For the case shown in Figure 25 where $E_o = 3.3$keV, $R/X_s = 45$ and the exponential term is equal to 0.001 at 80°. It is probable that the exponential term is not the reason for the divergence of theory and data for Figures 25, 26, and 27.

Figure 28 presents data and trajectory parameters for the case where $V(X) = 6150[1 - (X/B)^6]$, $E_p = 13$keV, $\sigma(0°) = 0.48$, and $\theta = 23°$ at $X = 0$. Any lateral shifting of the data points was unnecessary. Table 9 lists values of X, θ, V(X), sec(θ), the theoretical and experimental values for σ. At the high energy of 13keV there was little deviation of experiment from theory over the range from 23° to 38°. The data points rose monotomically as the edge of the specimen was approached and did not follow the theoretical predictions.

The reason that the theoretical curve in Figure 28 starts to drop off in the region 2 mm $\leq X \leq$ 3 mm is that the surface potential is dropping off in the region and therefore the secondary emission coefficient (for $\theta = 0°$) is also decreasing. The secondary emission coefficient (for $\theta = 0°$) in the region 2 mm $\leq X \leq$ 3 mm is approximated by Equation 23 where $\sigma = (E_c/E_o)^n$ and where $E_o = E_p - eA_o(1 - X/B)^6)$

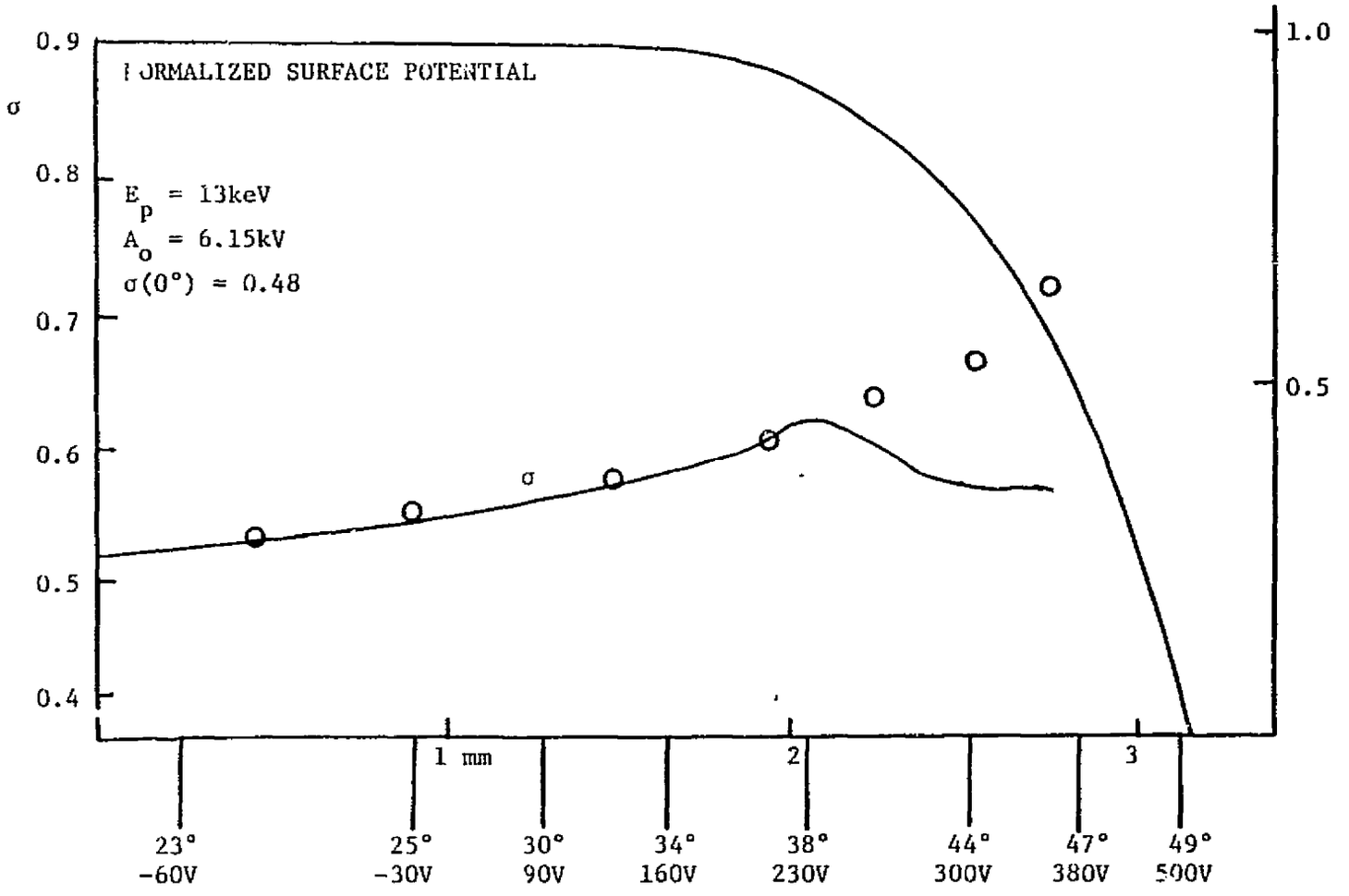

Figure 28. Comparison of experimental data with theory for E_p = 13.0keV and θ(X=0) = 23°. Trajectory parameters are indicated on the abscissa.

Table 9. Table of impact parameters for Figure 28 where $\theta = 23°$ at X=0 and $E_p = 7.2$keV.

X (mm)	θ (degrees)	V(X) (volts)	$\frac{1}{\cos\theta}$	σ theory	σ experiment
0.20	23	6150	1.09	0.52	0.53
0.91	28	6150	1.13	0.54	0.55
1.28	30	6120	1.15	0.56	0.58
1.66	34	6010	1.21	0.58	0.60
2.06	38	5670	1.27	0.61	0.62
2.49	44	4760	1.39	0.64	0.68
2.80	47	3200	1.47	0.55	0.70
3.03	49	1730	1.52	0.52	none

is the impact energy. As the surface potential falls, E_o increases which causes the decrease in σ over the region 2 mm $\leq X \leq$ 3 mm. The theoretical curve shows that σ is decreasing more rapidly than $\cos\theta$ is decreasing and therefore the theoretical value of σ decreases. The beam does not suffer much spreading at 47° and this effect, present in other experiments, is not the reason for the deviation of experimental data from the theoretical model outlined. In the region of disagreement it is possible that tangential electric fields are the reason that the experimental value of σ exceeds the theoretical value. It is interesting to note that in Figure 28 the experimental value of σ exceeds the theoretical value rather than the opposite as appears in Figures 25, 26, and 27. It is possible that for $\sigma < 1$ strong electric fields at the dielectric metal interface enhance secondary emission above the predicted theoretical values.

Grazing Incidence Measurements

The experimental results appearing in this section were obtained by probing the specimen near one of the edges at angles of incidence in the range of 45° to 75°. The experiments were conducted in the same manner as the experiment used to find σ for the case shown in Figure 25. The specimen surface was probed with the primary beam from the center to the edge of the specimen or to a point where no further signals were detected. A maximum experimental σ was obtained from each experiment as is indicated by the highest circle in each of Figures 25, 26, 27, and 28. Figure 29 summarizes the results obtained in this manner.

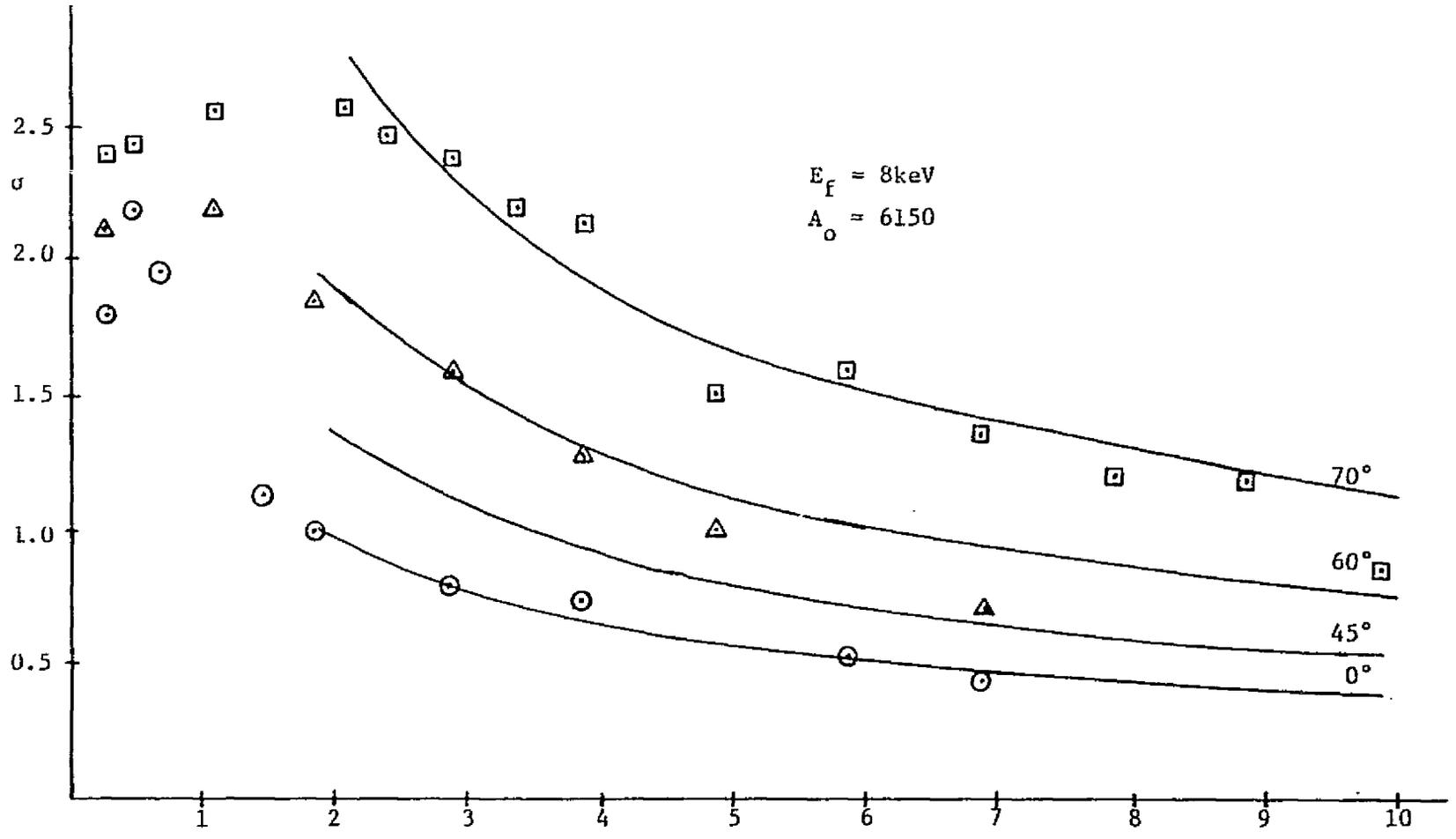

Figure 29. Plot of σ_{max} for grazing incidence experiments where the abscissa represents $E_p - eA_o$. The surface potential for this case was $V(X) = 6150(1 - (X/B)^6)$ and E_f = 8keV.

The value of σ for normal incidence is indicated in Figure 29 by the circles. Data points marked with a triangle are values of σ_{max} for those sets of trajectories which correspond to 23° incidence at the center of the specimen. Data points marked with a square are values of σ_{max} for the cases where the trajectories impacted the center of the specimen with an angle of 45°. In general each data point has a different angle of incidence θ. In the range of primary energies from 9keV to 16keV data points marked with squares are within $\pm$ 12° of θ = 70° and those marked with triangles are estimated to be within $\pm$ 10° of 45°. Justification for these limits is provided in the following text.

The abscissa represents the difference between the probing energy E_p and the peak surface potential energy eA_o while σ_{max} is indicated on the ordinate. The lowest solid curve is drawn through the normal incidence data while the upper three solid curves are obtained by dividing the values of σ at normal incidence by the cosines of 45°, 60°, and 70°, respectively. Table 10 shows the values of E_p, E_o, Q_m, Q_r, Q_p, and σ for each case plotted in Figure 29. A blank space in the table means no data was taken for the position indicated by that row and column. Columns three, four, five and six are for the normal incidence case; columns seven, eight, nine, and ten are for the points marked with triangles; and columns eleven, twelve, thirteen, and fourteen are for the data points marked with squares. The charges are in pC and the energies are in keV.

It is necessary to estimate the angle of incidence of all data points shown in Figure 29 as a triangle or square. The angles of incidence for the eight data points ($\theta \neq 0$) shown below the value

Table 10. Values of E_p, E_o, Q_m, Q_r, Q_p and σ for a surface potential where $V(X) = 6150[(1 - (X/B)^6]$.

		$\theta = 0°$			Triangle Data Points					Square Data Points			
E_p (keV)	E_o (keV)	Q_m (pc)	Q_r (pc)	Q_p (pc)	σ	Q_m (pc)	Q_r (pc)	Q_p (pc)	σ	Q_m	Q_r	Q_p	σ
6.4	.25	0.75	1.13	1.32	1.85	1.13	2.25	1.98	2.13	0.60	1.50	1.06	2.42
6.6	.45	0.72	1.50	1.26	2.19	--	--	--	--	0.74	1.85	1.28	2.45
6.8	.65	0.93	1.55	1.60	1.97	--	--	--	--				
7.2	1.05	--	--	--	--	1.41	2.75	2.34	2.25	0.86	2.25	1.43	2.57
7.6	1.45	6.00	1.25	9.80	1.15	--	--	--	--	--	--	--	--
8.0	1.85	--	--	--	1.00	1.70	2.00	2.68	1.75	--	--	--	--
8.2	2.05	--	--	--	--	--	--	--	--	1.85	4.70	2.95	2.59
8.5	2.35	--	--	--	--	--	--	--	--	2.00	4.70	3.15	2.49
9.0	2.85	4.40	1.50	6.80	0.78	1.60	1.50	2.47	1.61	1.70	3.70	2.63	2.40
9.5	3.35	--	--	--	--	--	--	--	--	1.33	2.44	2.02	2.21
10.0	3.85	3.13	1.65	4.70	0.65	2.25	0.93	3.28	1.28	1.50	2.60	2.25	2.15
11.0	4.85	3.80	2.30	5.55	0.58	--	--	--	1.00	2.00	1.50	2.92	1.51
12.0	5.85	2.90	2.00	4.14	0.52	--	--	--	--	1.50	1.20	2.14	1.56
13.0	6.85	3.13	2.20	4.30	0.49	4.40	1.86	6.16	0.70	1.80	0.90	2.52	1.36
14.0	7.85	--	--	--	--	--	--	--	--	3.75	1.10	5.16	1.21
15.0	8.85	--	--	--	--	--	--	--	--	6.30	1.50	8.55	1.18
16.0	9.85	--	--	--	--	--	--	--	--	4.40	1.00	6.10	0.83

of E_p = 9keV (or $E_p - eA_o$ = 3.85keV) were estimated to be about 80° yet no attempt is made to compare these data points to a theoretical model.

Table 11 shows the simulated angle of incidence θ for primary beam energies ranging from 9keV to 16keV for the data points associated with squares. Four cases are shown for each primary energy where each case has three parameters, the impact point X, the angle of incidence θ, and the surface potential V(X). Case one is shown in columns three and four where X ≈ 1.93 mm and V(X) ≈ 5900V. Case two is shown in columns five and six where X ≈ 2.15 mm and V(X) ≈ 5500V. Case three is shown in columns seven and eight where X ≈ 2.35 and V(X) ≈ 5100 while case four is shown in columns nine and ten where X ≈ 2.52 and V(X) ≈ 4600. The simulated impact points in Table 11 are like the impact parameters shown on the abscissa of Figures 25-28.

It should be noticed that any angles which are greater than 70° in Table 11 should be considered as experimentally impractical. This is due to the beam spreading effect which occurs as θ becomes large. For instance, when E_p = 9.5keV, X = 2.38 mm and θ = 75.8°. The beam width is about 0.6 mm. Information like that displayed in Table 11 was used to plot the theoretical curves shown in Figures 25 and 28. The values of θ listed in Table 11 provide the justification that the data points marked with squares in Figure 29 are within the limits of 70° $\pm$ 12°. Error bars for individual data points are smaller than $\pm$ 12° as Table 11 also indicates.

Table 12 compares the measured values of σ_{max} with the theoretical values of σ found for each of the four cases shown in Table 11. The theoretical values shown in Table 11 were found by computing the

Table 11. Values for E_p, $E_p - eA_o$, X , and θ for four separate cases where X = 1.95, 2.15, 2.35, 2.55, where θ(X = 0) = 45°.

V(X) ≈ 5900				V(X) ≈ 5500		V(X) ≈ 5100		V(X) ≈ 4600	
E_p (keV)	$E_p - eA_o$ (keV)	X (mm)	θ (degrees)	X (mm)	θ (degrees)	X (mm)	θ (degrees)	X (mm)	θ (degrees)
9.0	2.85	1.93	73.5	2.17	76.2	2.32	79.7	2.51	82.4
9.5	3.35	1.90	70.2	2.16	72.5	2.38	75.8	2.55	77.3
10.0	3.85	1.92	68.0	2.15	71.1	2.34	74.3	2.52	76.5
11.0	4.85	1.91	64.3	2.13	66.1	2.37	70.5	2.54	71.4
12.0	5.85	1.92	61.2	2.18	64.0	2.39	67.8	2.55	69.8
13.0	6.85	1.94	59.4	2.15	63.1	2.35	64.7	2.56	66.5
14.0	7.85	1.96	58.3	2.20	61.1	2.33	62.2	2.53	63.9
15.0	8.85	1.92	56.6	2.15	58.6	2.33	60.0	2.52	61.5
16.0	9.85	1.95	54.2	2.20	56.1	2.35	58.1	2.55	58.2

Table 12. Values for the E_p, $E_p - eA_o$, $\sigma(0°)$, σ_{max}, and σ for four separate impact cases where $V(X) = 6150(1 - (X/B)^6)$.

E_p (keV)	$E_p - eA_o$ (keV)	$\sigma(0°)$ experimental	σ_{max} experimental	σ X ≃ 1.95 (mm)	σ X ≃ 2.15 (mm)	σ X ≃ 2.34 (mm)	σ X ≃ 2.51 (mm)
9.0	2.85	0.78	2.40	2.67	2.98	3.41	4.61
9.5	3.35	0.72	2.20	2.13	2.36	2.65	2.44
10.0	3.85	0.65	2.15	1.73	1.95	2.23	2.25
11.0	4.85	0.58	1.51	1.37	1.40	1.56	1.56
12.0	5.85	0.52	1.55	1.07	1.14	1.27	1.31
13.0	6.85	0.48	1.36	0.94	1.01	1.02	1.07
14.0	7.85	0.44	1.21	0.83	0.89	0.87	0.88

value of the surface potential at each value of X and then approximating the value of σ for each case. For instance when X ≈ 1.95 mm the value σ(0°) = 0.72 is used when E_p = 9.5keV but for X ≈ 2.51 the impact energy is higher and σ is approximated as 0.58 even though E_p has not changed. The values of σ appearing in columns five through eight of Table 12 are found by dividing the adjusted values of σ(θ = 0°) by cos(θ) where each θ is found from Figure 11.

This complicated and laborious procedure was done so that the reader may compare various theoretical options with experiment. The author feels that the impact coordinate X = 2.15 is the point where maximum σ is most likely to occur, though the experimental procedure and apparatus did not allow the author to know exactly where that point occurred. The reason column six is the most reasonable choice is that the values of θ, for the cases where X ≈ 2.34 mm and X ≈ 2.51 mm, are so large and the impact points so close to the edge, that beam spreading would make σ smaller than it appears in columns seven and eight of Figure 12.

For the high primary energies of 12keV, 13keV, and 14keV, the theoretical values of σ appearing in columns five through eight of Figure 12 do not agree with the experimental value for σ_{max} regardless of impact coordinate choice. This is the same observation which was made in Figure 28. At 14keV no choice of X will provide a theoretical value of σ equal to the experimental value. This suggests that a primary beam with high impact energy and a large impact angle near a dielectric metal interface will possess a σ larger than theory would predict. At E_p as high as 15.5kV, the experimental value of σ_{max} is

unity where the impact angle, estimated from the simulations shown in Table 11, is 60°. The theoretically predicted critical voltage for 60° incidence is 7kV corresponding to E_p = 13kV.

Table 13 lists the same type of trajectory impact parameters as Table 11 except that this is the case for trajectories associated with triangles. Table 13 indicates that, at θ = 45°, V_c = 5kV where the inverse cosine law would predict a value of about 3.5kV. For grazing incidence near the dielectric metal interface the critical voltages measured were greater than those predicted by theory.

Figure 30 presents data similar to that presented in Figure 29. The data points marked with circles are for a normally incident primary beam while the data points marked with triangles are for probing beams which impact the surface at X = 0 with θ = 23°. The data points marked with squares are for trajectories which impact the center of the specimen with an angle of incidence equal to 45°. The surface potential in this case is $V(X) = 10040(1 - (X/B)^4)$ where the abscissa stands for $E_p - eA_o$. Table 14 lists the values of E_p, E_o, Q_m, Q_r, Q, and σ for each case outlined above. The solid line drawn through the circles is for the normal incidence case. The upper solid lines are constructed by dividing the normal curve by the cosines of 60° and 75° respectively. The peak value of $\sigma(\theta = 0°)$ appearing in Figure 30 is larger than the corresponding value of $\sigma(\theta = 0°)$ in Figure 29. The ratio of emission coefficients is about 1.14 for normal incidence and 1.27 for large angles of incidence. This indicates that higher emission coefficients are obtained at higher electric fields contrary to the work of Quoc-Nguyen (7).

Table 13. Values of E_p, $E_p - eA_o$, X and θ for three separate cases where X ≈ 1.90, 2.15, 2.35, where θ(X = 0) ≈ 23°.

E_p (keV)	$E_p - eA_o$	V(X) ≈ 5900 X (mm)	V(X) ≈ 5900 θ (degrees)	V(X) ≈ 5500 X (mm)	V(X) ≈ 5500 θ (degrees)	V(X) ≈ 5100 X (mm)	V(X) ≈ 5100 θ (degrees)
9.0	2.85	1.85	46.7	2.17	51.6	2.32	54.2
10.0	3.85	1.85	42.9	2.18	48.6	2.37	51.5
11.0	4.85	1.89	40.3	2.16	43.8	2.38	46.6
12.0	5.85	1.92	38.9	2.16	41.3	2.37	43.7
13.0	6.85	1.94	36.6	2.18	39.6	2.34	41.7

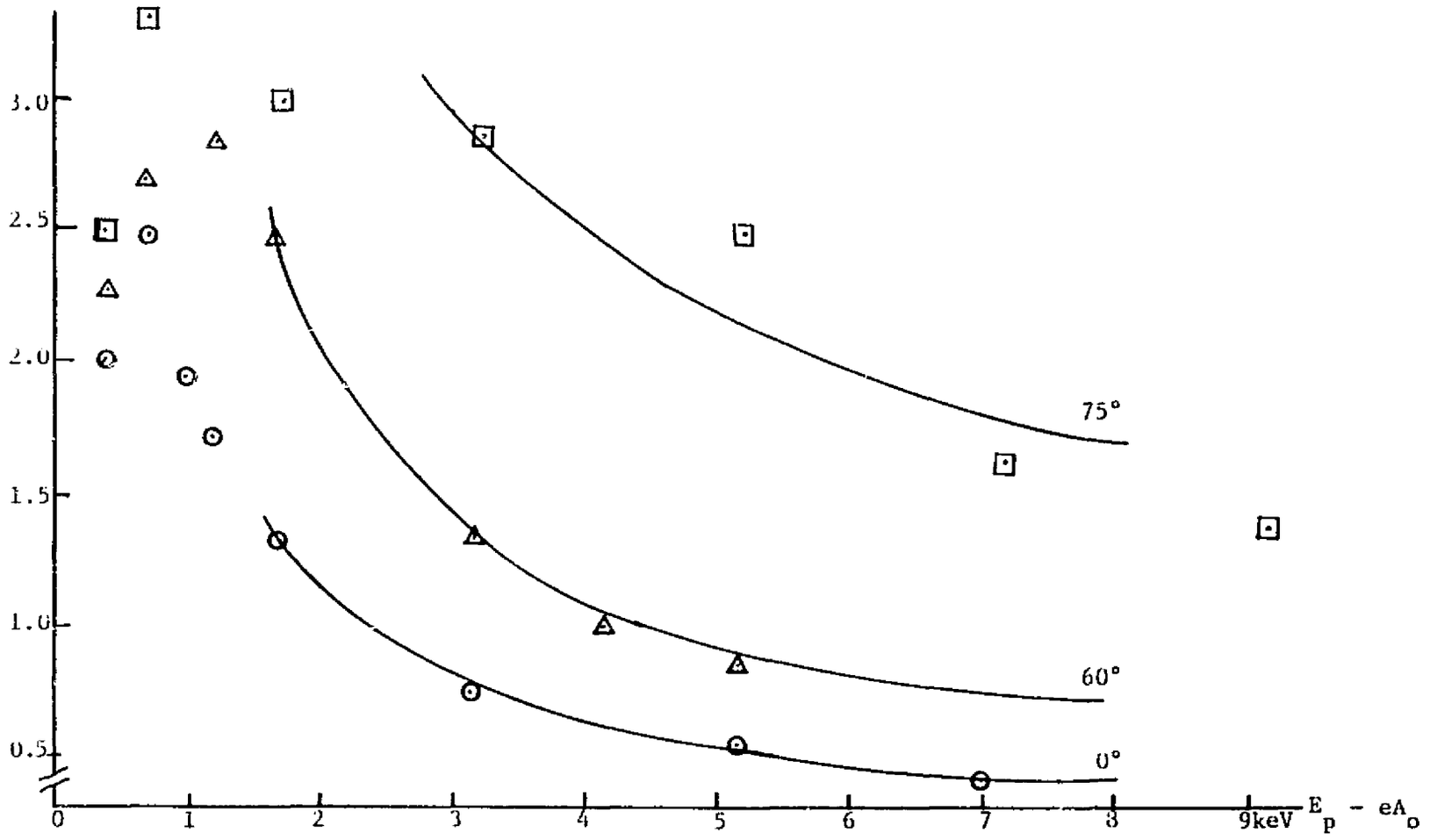

Figure 30. Plot of σ_{max} for grazing incidence experiments where the abscissa represents $E_p - eA_o$. The surface potential for this case was $V(X) = 10040(1 - (X/B)^4)$ and $E_f = 12keV$.

Table 14. Values of E_p, E_o, Q_m, Q_r, Q_p and σ_{max} for a surface potential of $10040[1 - (X/B)^4]$.

		$\theta = 0°$				Triangle Data Points				Square Data Points			
E_p (keV)	E_o (keV)	Q_m (pC)	Q_r (pC)	Q_p (pC)	σ	Q_m (pC)	Q_r (pC)	Q_p (pC)	σ	Q_m (pC)	Q_r (pC)	Q_p (pC)	σ
10.4	.36	1.50	2.30	2.20	2.00	0.94	1.60	1.40	2.20	0.90	2.00	1.35	2.50
10.7	.66	1.70	3.80	2.50	2.50	0.88	2.20	1.30	2.70	0.75	2.50	1.00	3.30
11.0	.96	1.50	2.10	2.20	2.00								
11.2	1.16	2.60	2.80	3.80	1.70	1.30	3.50	1.90	2.90				
11.7	1.66	3.20	1.50	4.60	1.30	1.00	2.00	1.40	2.50	1.30	3.80	1.90	3.00
12.2	2.16												
13.2	3.16	6.00	2.00	8.70	0.76	7.40	3.70	10.7	1.30	0.96	2.50	1.34	2.90
14.2	4.16								1.00				
15.2	5.16	6.80	7.10	9.20	0.55	9.00	1.80	12.2	0.86	1.00	2.00	1.35	2.50
17.2	7.16									1.30	1.50	1.70	1.90
19.2	9.16	6.40	6.30	8.20	0.48					1.40	0.68	1.80	1.40

Table 15 parallels for the higher surface potential what were presented in Tables 11 and 12 for the lower potential. Column one represents the primary energy, column two represents some assumed impact points corresponding to σ_{max}, column three is the angle of incidence for the assumed impact point, column four is the potential at the impact point, column five is the measured value of σ for normal incidence, column six is the measured value of σ_{max} and column seven is the theoretical value of σ_{max} (θ). Here $E_p - eA_o$ is only about 5keV (for E_p = 15.2keV) whereas in Table 13 $E_p - eA_o$ was about 8keV; therefore Table 15 does not represent the very high impact energies as does Table 12.

Table 15. List of values of E_p, X, θ, V(X), $\sigma(0°)$, measured σ, and calculated σ for the surface potential $V(X) = 10040(1 - (X/B)^4)$.

E_p	X (mm)	θ (degrees)	V(X) (volts)	$\sigma(0°)$	$\sigma(\theta)$ measured	$\sigma(\theta)$ calculated
11.7	1.27	77.2	9800	1.30	3.0	5.87
13.2	1.53	72.6	9500	0.76	2.9	2.54
15.2	1.54	65.1	9500	0.55	1.35	1.30

CHAPTER V

SUMMARY AND CONCLUSIONS

Basically two experimental cases were investigated: (1) measurements of σ were conducted in the presence of normal electric fields near the center of the specimen, and (2) measurements of σ were made at grazing incidence near the edge of the specimen where tangential fields were at least as strong as the normal field.

Normal Incidence and Normal Fields

Values of the critical voltage (the voltage spread between the two $\sigma = 1$ points) were measured for normally incident electrons where the flood gun charging potential V_f was equal to 6kV, 8kV, 10kV, 12kV, and 14kV. The secondary emission coefficient was measured for two cases where E_f was 8kV and 12kV, and where the peak surface potential A_o was equal to 6150V and 10040V respectively. When the peak surface potential was 6150V the normal electric field was 1500V/mm and when A_o = 10040V the normal field strength was 2730V/mm. The exponent n (= 0.58) which characterizes high energy behavior of σ, as stated in Equation (23), was determined for an uncharged specimen. This value of n seemed to hold equally well in the case of charged specimens.

Oblique Incidence and Normal Fields

In Figures 25, 26, 27, and 28 experimental data indicated that in the presence of normal electric fields and angles of incidence up

to 60° the experimental results agreed with the simple inverse cosine law.

Oblique Incidence and Non-Normal Fields

The section relating to measurements of σ_{max} could not be modelled accurately because the impact point was difficult to specify. However, the secondary emission coefficient did not in general obey the inverse cosine law at high energies (E_p > 12kV) and in regions of strong tangential fields. The emission coefficient was greater than that predicted. Values of critical energy were also bigger than the inverse cosine law predicted.

Conclusions

In the presence of normal electric fields and impact energies E_o > 500V the inverse cosine law for secondary emission is a good model for the behavior of obliquely incident electrons. In the presence of strong tangential fields near a dielectric metal interface σ seems to be consistently larger than it is modelled to be at high primary energies.

REFERENCES

1. Katz, D. E., et al. "A three dimensional dynamic study of electrostatic charging in materials," NASA CR-135256, August 1977.

2. Robinson, J. W. "Surface charge kinetics near metal-dielectric interfaces exposed to kilovolt electron flux," Final Report, NASA Grant NSG-3097, Sept. 1977.

3. Robinson, J. W.; & D. G. Tilley. "Potential mapping with charged particle beams," Spacecraft Charging Technology--' 78, AFGL-TR-79-0082, pp. 606-620, October 31-November 1, 1978.

4. Robinson, J. W. "Mapping of electrical potential distribution with charged particle beams," Semi-annual Report, NASA Grant NSG-3166, July 1979.

5. Robinson, J. W.; & P. A. Budd. "Mapping of electrical potential distribution with charged particle beams," Semi-annual Progress Report, March 1980, NASA Grant No. NSG-3166.

6. Tilley, D. G. "Dipole and quadropole synthesis of electric potential fields," Technical Report, NASA Grant NSG-3166, July 1979.

7. Quoc-Nguyen, N. "Secondary electron emission from a dielectric film subjected to an electric field," NASA CR-155213, November 1977.

8. Robinson, J. W. "Mapping of electrical potential distribution with charged particle beams," NASA Grant NSG-3166, Sept. 1980.

9. Beers, B. L., et al. "Electron transport model of dielectric charging," Proceedings of the USAF/NASA Spacecraft Charging Technology Conference, 1978.

10. Harrower, G. A. "Energy spectra of secondary electrons," Physical Review, vol. 104, p. 52, 1956.

11. Dobretsov, L. N.; & M. V. Gomoyunova. Emission Electronics. Israel Program for Scientific Translations, Jerusalem (Translated from Russian by I. Shechtman, pp. 235-292).

12. Fridrickhov, S. A.; & A. R. Shulman. "An investigation of the secondary electron emission by certain dielectrics at low primary electron energy," Soviet Physics Solid State, vol. 1, no. 8, p. 1153, 1960.

13. Bronshtein, I. M.; & R. B. Segal. "An investigation of electron reflection from certain metals," Soviet Physics Solid State, vol. 1, p. 1365, 1960.

14. Martsinovskaya, E. G. "Secondary electron emission from some aromatic hydrocarbons," Soviet Physics Solid State, vol. 7, no. 3, p. 661, September 1965.

15. Kanter, H. "Energy dissipation and secondary electron emission in solids," Physical Review, vol. 121, no. 3, p. 677, Feb. 1, 1961.

16. Lye, R. G.; & A. J. Dekker. "Theory of secondary emission," Phys. Rev., vol. 107, no. 4, Aug. 15, 1957, pp. 977-981.

17. Willis, R. F.; & D. K. Skinner. "Secondary electron emission yield behavior of polymers," Solid State Communications, vol. 13, pp. 685-688, 1973.

18. Dekker, A. J. Solid State Physics. Prentice-Hall, Inc., 1959.

19. Bruining, H., M.B.E. Physics and Applications of Secondary Electron Emission. McGraw-Hill Book Company, Inc., 1954.

20. Katz, D. E., et al. "A three dimensional dynamic study of electrostatic charging in materials," NASA CR-135256, August 1977.

21. Jonker, J. L. H. "On the theory of secondary electron emission," Philips Research Reports, vol. 7, pp. 1-20, 1952.

22. Everhart, T. E. "Simple theory concerning the reflection of electrons from solids," Journal of Applied Physics, vol. 31, no. 8, Aug. 1960.

23. Gibbons, D. J. "Secondary electron emission," Handbook of Vacuum Physics, vol. 2, p. 299, Pergamon, 1966.

24. Dekker, A. J. "On the escape mechanism of secondary electrons from insulators," Physica, vol. 21, p. 29, 1954.

25. Young, J. R. "Penetration of electrons in aluminum oxide films," Physical Review, vol. 103, p. 292, 1956.

26. Young, R. J. "Dissipation of energy by 2.5-10keV electrons in Al_2O_3," Journal of Applied Physics, vol. 28, no. 5, May 1957, p. 524.

27. Johnson, J. B.; & K. G. McKay. "Secondary electron emission of crystalline MgO," Physical Review, vol. 91, no. 3, p. 582, Aug. 1, 1953.

28. Whetten, N. R.; & A. B. Laponsky. "Secondary electron emission from MgO thin films," Journal of Applied Physics, vol. 30, no. 3, p. 432, March 1959.

29. DeVogelaire, R. "A method for the numerical integration of differential equations of second order without explicit first derivatives," Journal of Research of the National Bureau of Standards, 54, p. 119, March 1955.

30. Jackson, J. D. Classical Electrodynamics. Wiley, 1962.

APPENDIX A

DETERMINATION OF DEFLECTION FACTOR

APPENDIX A

The deflection factor D is defined to have the units of radians per volt. It is a measure of the angle with respect to a normal drawn outward from the cylinder exterior (angle β). By adjustment of the deflection voltage various angles of incidence may be given to the probing beam.

The probing beam is deflected at some point outside of the cylinder by the deflection plates. This point was found to be 1.0 cm from the exterior of the cylinder. This point was found experimentally to be fixed regardless of probing beam potential. The point of deflection was found by measuring electron trajectories through the frontside and backside of the cylinder for specific deflection voltages as shown in Figure 31.

Figure 31 shows two probing beam trajectories which pass through the cylinder when the platform has been removed. The entry and exit points are found for constant deflection voltages DV_1 and DV_2. Straight lines are drawn through these points and the angle that is subtended by these lines is called 2Ψ. The difference of the deflection voltages $(DV_1 - DV_2)$ is divided by 2Ψ and yields a quantity we will call G.

It is necessary to introduce a correction factor to the quantity G in order to obtain D, the deflection factor. Figure 32 shows the geometry considered. The angle Ψ is shown as in Figure 31 and β, the probing beam angle of inclination, is also shown. An analysis of the geometry using the law of sines and the fact that the cylinder radius is 2.54 cm and that the distance from cylinder to point of deflection is 1.0 cm it is possible to estimate β given Ψ. This analysis states

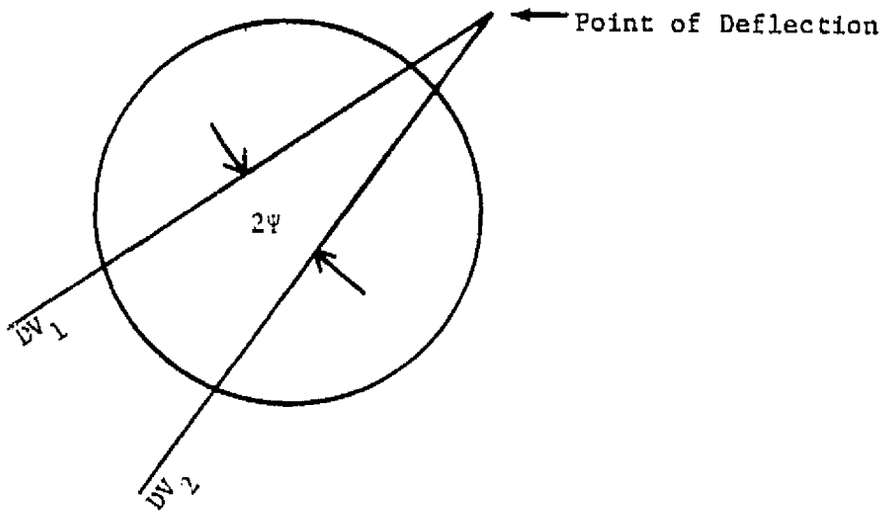

Figure 31. Figure showing two trajectories through the cylinder for two different deflection voltages and the angle subtended by the trajectories, Ψ.

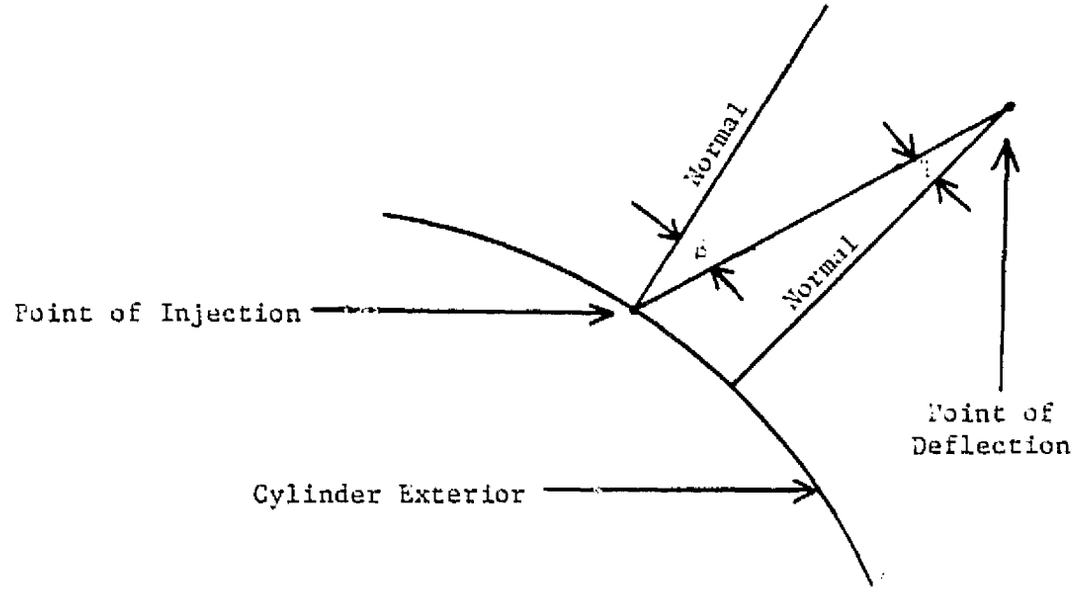

Figure 32. Figure showing how δ is obtained from Ψ.

that for Ψ and β small it is sufficient to multiply Ψ by 1.4 to obtain the correct angle of inclination β. The angle β was one of the two angles used as input parameters to the computer simulations.

Table 16 shows G for each probing beam energy E_p and the product of the two. It was sufficient to multiply G by 1.4 in order to obtain D.

Table 16. Values for probing beam energy, deflection factor G, and the product of G and E_p.

E_p keV	G milliradians/G	G x E_p
3	.512	1.57
3.5	.444	1.55
5	.312	1.57
7	.230	1.61
8	.216	1.73
12	.145	1.69
14	.126	1.78

APPENDIX B

PROCEDURE FOR CHARGING SPECIMEN

APPENDIX B

The following procedure was implemented in order to charge the specimen to a known potential with the system flood gun.

(1) Turn high voltage power supply to zero.

(2) Set high voltage switch in the position to power flood gun.

(3) Rotate cylinder to the position where the charging window is between the platform and the flood gun.

(4) Rotate the platform from some arbitrary position to the position where it is perpendicular to the flood gun beam.

(5) Turn electrometer to the proper setting (Coulomb mode) such that the anticipated measurements do not read off scale.

(6) Release electrometer needle lock.

(7) Turn up high voltage power supply to the desired flood gun potential.

(8) Turn up flood gun filament current and wait until charge monitored by electrometer stabilizes.

(9) Turn off flood gun filament current.

(10) Rotate platform and cylinder to positions for the coming experiment.

(11) Turn high voltage power supply to zero.

(12) Turn high voltage power switch to the position which powers the probe gun.

APPENDIX C

PROCEDURE TO FIND THE TEST CHARGE

APPENDIX C

The following step by step procedure was used in order to find the amount of test charge Q_m.

(1) Set platform perpendicular to the probing beam and the cylinder at a position where the detector wires do not obstruct the beam.

(2) Set high voltage power switch to the position which powers the probing beam.

(3) Set V_H in pulse circuitry to about 1KV and set V_L at the voltage desired for each specific experiment. Set pulse width as desired.

(4) Switch the electrometer to 10^{-10}C with a multiplier setting of 0.03.

(5) Turn high voltage switch to the position which powers the probing beam.

(6) Turn up the high voltage power supply to the probing beam potential desired.

(7) Turn on strip recorder to speed of 20 mm/s.

(8) Release needle lock on electrometer.

(9) Close switch one in pulse circuitry and lock needle on electrometer.

(10) Label each recording and record (a) beam energy, (b) motor settings, (c) pulse width, (d) V_H and V_L, (e) electrometer settings.

(11) Continue pulsing specimen with various voltages V_L.

(12) Turn down high voltage power supply.

APPENDIX D

PROCEDURE FOR DISCHARGING SPECIMEN

APPENDIX D

The following procedure was implemented in order to discharge the dielectric specimen.

(1) Turn high voltage power supply to zero.

(2) Switch high voltage power to the flood gun.

(3) Rotate platform to the position where it is perpendicular to the flood gun beam.

(4) Rotate cylinder until the window is between the specimen and flood gun.

(5) Set electrometer to read positive charge on 10^{-6}C scale and release needle lock.

(6) Turn up high voltage power supply to the potential at which the specimen was last charged.

(7) Turn up flood gun filament current.

(8) Slowly (500 V/s) decrease high voltage to zero volts while monitoring charge on electrometer.

(9) Turn flood gun filament current to zero.

(10) Compare the positive charge released to the negative charge deposited and continue if charges are equal. If the charges are unequal go back to (6).

APPENDIX E

PROCEDURE FOR FINDING $\sigma(\theta = 0°)$

APPENDIX E

The following procedure was implemented in order to find σ for normally incident electrons.

(1) Charge specimen and lock needle on electrometer.

(2) Set high voltage power supply at zero volts and apply this voltage to the probing beam.

(3) Set V_H and V_L as desired for specific experiment.

(4) Set electrometer on 10^{-10}C scale and use appropriate multiplier setting (0.01, 0.03).

(5) Turn up high voltage power supply to the desired potential corresponding to the voltage used in Appendix C.

(6) Check drift rate on electrometer to see which multiplier setting is best (0.01, 0.03).

(7) Turn strip recorder tape speed on (20 mm/s), release needle lock, pulse deflection voltage, quickly push in needle lock and turn off strip recorder tape drive.

(8) Record V_L, V_H, pulse width, motor settings, flood potential, probe potential, and electrometer settings for each measurement.

(9) Repeat eight for various low voltages V_L.

APPENDIX F

MEASUREMENT OF REFLECTED TRAJECTORIES

APPENDIX F

The following procedure was used in order to measure reflected trajectories used in potential mapping.

(1) Charge specimen to V_f.

(2) Switch high voltage switch to probe beam position.

(3) Rotate platform to the position where it is perpendicular to the probing beam.

(4) Rotate cylinder to the position where the detector wire is 1° from an undeflected probing beam entering the cylinder.

(5) Turn probing beam potential to 3KV below V_f.

(6) Vary deflection voltage until the detector wire has been struck and record that deflection voltage. No beam pulsing is used.

(7) Set detector wire at γ = +54°, +36°, +18°, -18°, -36°, and -54° and record the deflection voltages required to strike the detector wires with the reflected probing beam.

(8) Record V_f, V_p, and the various deflection voltages.

(9) Turn down high voltage supply to zero.